Macromolecular crowding effects on the excited-state dynamics of novel FRET probes using time-resolved fluorescence

A Thesis
SUBMITTED TO THE FACULTY OF
UNIVERSITY OF MINNESOTA
BY

Jacob A. Schwarz

IN PARTIAL FULFILLMENT OF THE REQUIREMENTS
FOR THE DEGREE OF
MASTER OF SCIENCE

Dr. Erin D. Sheets

August 2017

Acknowledgements

I would first like to thank Dr. Erin Sheets and Dr. Ahmed Heikal, for their continuing supports and guidance throughout the last two years. Not only did they keep me in the right direction, they also made it a joy to be in the lab and work with them and my fellow colleagues.

I would also like to thank all of the people in the Sheets and Heikal Labs, who have helped along the way with this project. Hong Bok Lee, Ryan Leighton, Ntsang Anye, Alex Naughton, Gerald Sakamaki, Nathan Korson, Kaelt Simpson and Claire Baetzold. All of these colleagues have engaged in collaboration allowing me to think freely and challenge me to take the next step. I also would like to extend a big thank to Megan Currie, who did a lot of the pioneer research into this project allowing for this research to move forward quickly.

Also, a thank you to our collaborator, Dr. Arnold J. Boersma, of the University of Groningen the Netherlands, who generously supplied the DNA for the FRET probes used in this project.

Ben Orpen and Christian Coffman in the Hinderliter Lab were a big help in their technical support of steady-state fluorescence collection, without their assistance we would not have progressed nearly as fast, so to them a thank you.

I would also like to thank all of the generous funding sources, the University of Minnesota Duluth Department of Chemistry and Biochemistry, Swenson College of Science & Engineering, University of Minnesota Grant-in-Aid, University of Minnesota Duluth Chancellor's Small Grant, the Minnesota Supercomputing Institute and the University of Minnesota, and the Netherlands Organization of Scientific Research Vidi grant.

Finally, I would like to thank Hannah Leopold. I have never met someone with as much work ethic, intellect, and wit, all bundled into one person.

Dedication

To Bella and Ralphie,

for keeping the sanity within the lab.

Abstract

Living cells are crowded with large molecules (proteins and nucleic acids) and organelles. These macromolecules are known to have many effects on cellular processes, yet there is still a need to develop a technique to quantify crowding concentrations in live cell studies. Recently, several fluorescence-based probes have been engineered to potentially quantify crowding within living cells. These dynamic probes contain a pair of fluorophores (mCerulean3 and mCitrine, the donor and acceptor, respectively) that are capable of fluorescence resonance energy transfer (FRET). This series of probes are connected by a linker of variable length and rigidity that allow them to undergo varying degrees of conformational changes upon increases in macromolecular crowding. Due to the newness of these FRET probes, there is a need to characterize the excited-state dynamics of these new protein-based sensors using fluorescence techniques that are compatible with non-invasive and imaging modes. Here we used steady-state spectroscopy and time-resolved fluorescence to accomplish this characterization. We also used cleaved versions of these probes to control for complexities resulting from changes in refractive indices. These measurements allow us to develop a kinetic model for the depopulation of the donor's excited-state, and to estimate the FRET efficiencies of these probes in both heterogeneous and homogenous environments. We find that these probes undergo conformational changes in heterogeneous environments and favor a more compact structure, thereby increasing energy transfer rates. Conversely, in homogenously viscous environments, our probes do not favor conformational changes when compared to pure buffer solutions. These results serve as the next advancement in developing the full potential of these probes for future studies in live cells.

Table of Contents

Appendices

List of Tables

List of Figures

List of Abbreviations

FCS	fluorescence correlation spectroscopy
FLIM	fluorescence lifetime imaging microscopy
FRET	fluorescence resonance energy transfer
NA	numerical aperture
NMR	nuclear magnetic resonance
PBS	phosphate buffered saline
SRF	system response function
TCSPC	time-correlated single photon counting

List of Symbols

A_1	pre-exponential factor for population capable of FRET
A_2	pre-exponential factor for population incapable of FRET
c	constant
E	energy transfer efficiency
F_D	fluorescence intensity of donor alone
F_{DA}	fluorescence intensity of donor in the presence of acceptor
$J(\lambda)$	spectral overlap
k_{et}	rate of energy transfer
k_{fl}^{D}	rate of fluorescence for donor alone
$k_{non\text{-}rad}$	rate of non-radiative processes
k_{rad}	rate of radiative processes
n	refractive index
N_1	population on fluorophores incapable of FRET
N_2	population of fluorophores capable of FRET
N_{total}	total population of an ensemble
Q_D	quantum yield
R_0	Förster distance
R_{da}	distance between donor and acceptor fluorophores
t	time
κ^2	orientation parameter
λ	wavelength
χ^2	chi- squared
τ_D	fluorescence lifetime of donor alone
τ_{DA}	fluorescence lifetime of donor in the presence of acceptor

Chapter 1
Introduction

1.1 Overview

Disclosure: This Chapter has been published, in part, in the following:

Currie, M., Leopold, H., Schwarz, J., Boersma, A., Sheets, E.D., Heikal, A.A. (2017) "Fluorescence Dynamics of a FRET Probe Designed for Crowding Studies" *Journal of Physical Chemistry (B)*.

Cells are crowded with macromolecules causing effects in cellular processes (1, 2). Mechanisms, such as the depletion attraction, of how crowding influences cells have been around as early as 1958 (3, 4), yet many studies investigating cellular processes are still done in dilute solutions and therefore may not be a viable representation of living cellular environments. For this reason, macromolecular crowding effects are under intense investigation. Recent studies on crowding have used single-particle tracking (5), NMR spectroscopy (6-8), fluorescence correlation spectroscopy (FCS) (5, 9, 10), and time-resolved anisotropy (11-14). Additionally, fluorescence resonance energy transfer (FRET) can be used as a probe to provide insight into conformational changes and interactions of biomolecules (15-23). Other techniques using FRET, include but are not limited to multichannel confocal microscopy (24), fluorescence lifetime imaging microscopy (FLIM) (25), steady-state fluorescence (26), and total internal reflection fluorescence (27). Even though these investigations into macromolecular crowding develop new understandings, quantification of macromolecular crowding during *in vivo* studies remains challenging.

1.2 Effects of macromolecular crowding in cells

The presence of macromolecules limiting the volume available to proteins and other solutes within cells is believed to affect equilibrium concentrations (2), aggregation (28), and diffusion rates (2, 29, 30). The concentrations of macromolecules is highly dependent on environmental factors, such as the location within a cell, and are believed to range between 80–300 g/L (2). Several recent studies investigating specific biological processes are now including crowding as essential for accurate, representative cellular

environments. The differences in kinetics and equilibria can be on the orders of magnitude different when compared to the same processes in uncrowded, buffer solutions (2).

Macromolecular crowding effects occur when the volume within an environment is limited by the presence of macromolecules; that is, excluded volume. Macromolecular crowding effects can vary widely because they not only depends heavily on size, shape, and the number of macromolecules present, but also the size and shape of the molecules under investigation (29). However, excluded volume only accounts for part of the crowding effects. Weak interactions also play an important role in crowding phenomena, such as hydrogen bonding, surface charges, and changes in entropy (4, 31, 32).

1.3 Macromolecules used for crowding studies

Macromolecules typically used to simulate crowding *in vitro* vary largely in shape and size. Many different polymers, such as polyethylene glycol, Ficoll, and dextran, are routinely used to mimic crowding, because they are highly water soluble, non-toxic to cells, are produced with high purity, and can be easily purchased in a variety of sizes, all of which are necessary characteristics of ideal crowding agents (2). Large proteins, such as ovalbumin and bovine serum albumin, are also often used in crowding studies, which not only create excluded volume effects but also more varied soft interactions due to the presence of surface charges (2, 33-36).

It is also important to distinguish between heterogeneous and homogenous environments (37). Heterogeneous environments are described in this Thesis as environments that contain large, inert, molecules, and between these molecules, are small pockets of buffer-like environments. Heterogeneous environments also induce changes in bulk viscosity, and so it is important to have proper controls when studying heterogeneous environments to ensure distinction between the effects of viscosity and crowding. Homogenous environments are created when the micro and bulk viscosities are the same, in addition to the solvent molecules being much smaller than the solute molecules. Previous studies have used small molecules, such as glycerol or sucrose, in buffer to create environments with homogenous viscosities under investigation (21).

In this work, we used Ficoll-70, to create heterogeneous environments. This polymer is inert and can best described via a hard sphere model. As a control, we also used the different concentrations of glycerol to create homogenous viscosity. It is now becoming common practice to crowd solutions with macromolecules for studies done *in vitro*; however, there is still no practical way to quantify crowding in living cell studies. Recently, several sensors have been developed with the potential of solving this problem (21, 38).

1.4 Introduction to FRET probes

The probes that are investigated in this Thesis are capable of undergoing FRET, which was used to quantify macromolecular crowding *in vitro* through changes in FRET efficiency. Importantly, all of the constructs we have investigated, shown in Figure 1.1, have the same donor-acceptor pair namely, mCerulean3 (39) (donor) and mCitrine (acceptor), but differ in the length and structure of their respective flexible linker regions (21). The two main structures within these construct's linkers are the loop regions defined by the $(–GSG–)_n$ sequence which are more flexible than the α-helix structures defined by the $(–EAAAK–)_m$ sequence.

It is also critical to understand the complexity of using fluorophores, derived from naturally occurring green fluorescent protein. The genetic modifications used to make mCerulean3 and mCitrine have been used to modify the fluorescence properties towards improved photostability, single exponential decays, and increased quantum yields (39). Both of these fluorophores have also been encoded with a A206K mutation to prevent dimerization (39, 40). However even with this mutation, mCitrine has been found to dimerize when above micromolar concentrations, however, for our experiments, the concentrations were well below this at nanomolar concentrations (41), thereby making this complication negligible.

Previous studies have used steady-state fluorescence to assess the energy transfer efficiency of these probes (21, 38); however, this technique is limited to bulk studies, preventing imaging capabilities. In addition, steady-state spectroscopy approaches suffer from complications in accuracy due to spectral overlap and inability to accurately

measure conformational changes (42, 43). In this Thesis, we use time-resolved fluorescence lifetime measurements, which are compatible with imaging modes in future studies, to quantify changes in FRET efficiency as a function of crowding. These probes also have the ability to be genetically encoded within *E. coli* and mammalian cell lines, allowing for future *in vivo* studies. By characterizing these constructs in the well-controlled environments of bulk solutions, and by using a technique compatible with non-invasive imaging, we come closer to resolving the issue of quantifying macromolecular crowding *in vivo*.

1.5 Steady-state fluorescence and lifetime measurement

Many studies involving quantification of FRET efficiency rely on the two main techniques of steady-state fluorescence and time-resolved lifetime decay measurements (44, 45). Using Eqs. 1.1 and 1.2 for steady-state fluorescence and fluorescence lifetime respectively, we can use either technique to quantify FRET efficiency (46). These calculations use the relative intensity (F) and lifetime (τ) of the donor in the presence (F_{DA}, τ_{DA}) and absence (F_D, τ_D) of acceptor to determine how much energy transfer has occurred. These equations are more thoroughly described in Section 2.6.

$$E(\%) = 100\left(1 - \frac{F_{DA}}{F_D}\right) \tag{1.1}$$

$$E(\%) = 100\left(1 - \frac{\tau_{DA}}{\tau_D}\right) \tag{1.2}$$

As with every experimental technique, steady-state fluorescence and fluorescence lifetime have their respective advantages and disadvantages. Steady-state spectroscopy is incapable of imaging and can be inaccurate due to spectral overlap, whereas, lifetime measurements can be complicated by the sensitivity of t_{DA} and t_D to refractive index (15-18), multi-exponential decays of fluorophores (46), and many other environmental factors (47). Further descriptions of these complexities are discussed in Section 2.6.

1.6 Summary

We hypothesize that these FRET probes will undergo conformational changes, favoring a compact conformation in the presence of macromolecular crowding, which would lead to enhanced FRET efficiency. Additionally, we hypothesize that the conformations of these probes will be independent of homogenously viscous environments due to limited thermal fluctuations.

In this work, we investigate these probes to further understand their individual potential for use as a practical *in vivo* macromolecular sensor. Using time-resolved fluorescence lifetime measurements, we examine the excited-state dynamics of the five FRET constructs as a function of wavelength and as a function of heterogeneous and homogenous environments. Using multiple wavelengths for excitation and detection, we were also able to develop a kinetic model to describe these hetero-FRET systems.

The topics discussed in this Thesis are as follows: in Chapter 2, materials, methods, and experimental rationale are described in detail. Chapter 3 discusses steady-state fluorescence measurements used to inform further experimental design, such as excitation and detection wavelengths. Chapter 4 describes the theoretical modeling of fluorescence lifetime decays, and experimental data that were used to validate the models. Chapter 5 discusses the wavelength dependence and differences in linker length and structure between constructs. Chapter 6 characterizes the FRET constructs in both heterogeneous and homogenous environments. Finally, Chapter 7 describes the conclusions and future directions of this project.

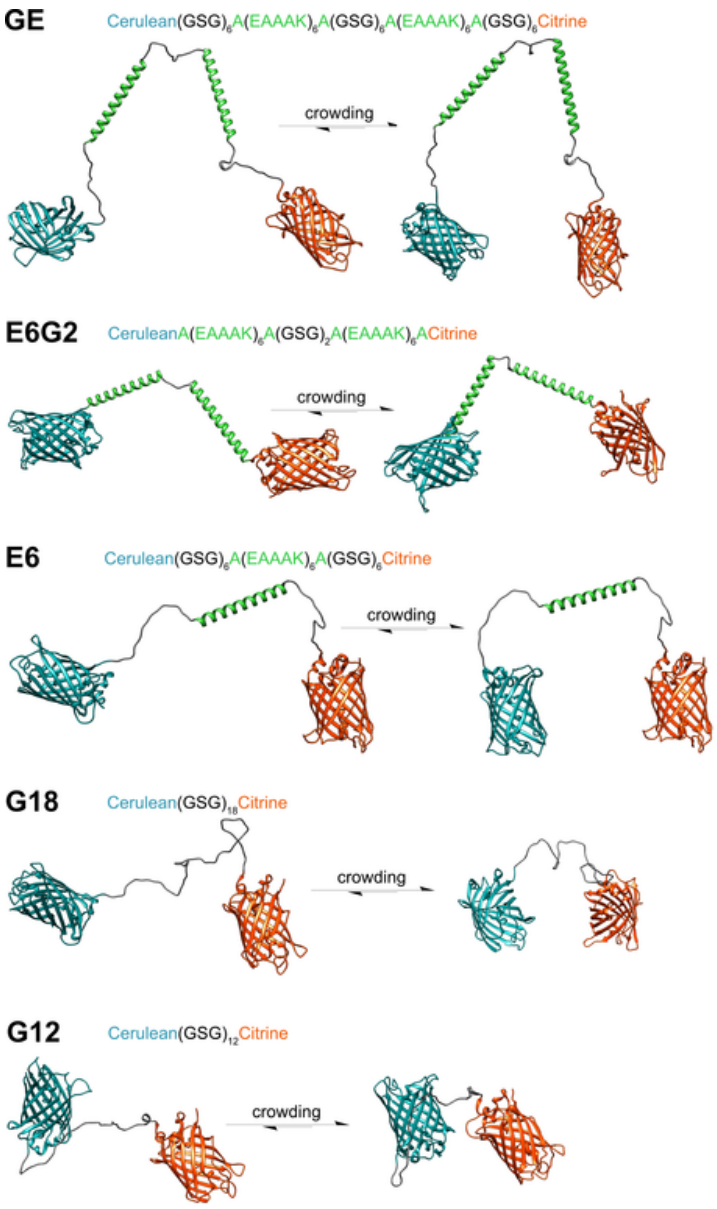

Figure 1.1: Constructs of FRET probes for quantification of macromolecular crowding.

Chapter 2

Materials and Methods

2.1 Overview

Disclosure: This Chapter has been published, in part, in the following:

Currie, M., Leopold, H., Schwarz, J., Boersma, A., Sheets, E.D., Heikal, A.A. (2017) "Fluorescence Dynamics of a FRET Probe Designed for Crowding Studies" *Journal of Physical Chemistry (B).*

This Chapter describes the constructs, purification and cleavage. Optical setup and corresponding theory used for data collection and analysis for the investigation of the excited-state dynamics for our crowding sensors is also discussed.

2.2. Construct purification

Plasmids in the parent pRSET A vector were generously provided by Arnold J. Boersma (University of Groningen, the Netherlands). These plasmids were transformed into the *E. coli* strain, BL21(DE)pLysS, and stored at –80°C as frozen cell stocks.

Bacteria were grown in terrific broth that had been supplemented with 0.4% (v/v) glycerol and 1 mg/mL ampicillin until the absorbance at 600 nm reached 0.060 on the NanoDrop 2000 spectrophotometer (Thermo Scientific). Protein production was induced with 0.1 mM isopropyl-β-D-thiogalactoside and incubated for 18 hours at 25°C. The cells were pelleted (Beckman J25.5, 3000 × g , 5000 rpm, 5 min, 4°C), resuspended in lysis buffer (10 mM sodium phosphate, pH 7.4, 100 mM sodium chloride, 0.1 mM phenylmethylsulfonyl fluoride, 1 mg/mL lysozyme), and allowed to incubate on ice for 30 min. Cells were lysed via probe sonication (Branson Sonifier 450, 10 s, level 7, 50% duty cycle, followed by 10 s incubation on ice, done 6 times). Cells were further lysed using an 18.5 gauge needle to draw up the lysate five times, and incubated on ice for 60 min.

After centrifuging lysed cells to remove cell debris (Beckman J25.5, 3000 × g, 5000 rpm, 15 min, 4°C), imidazole was added to a final concentration of 10 mM, and the

lysate was poured onto a ProBond Ni^{2+}-based affinity column that had been previously equilibrated with binding buffer (10 mM sodium phosphate, pH 7.4, 100 mM sodium chloride, 10 mM imidazole). The column was then washed four times with wash buffer (50 mM sodium phosphate, pH 8.0, 300 mM sodium chloride, 20 mM imidazole). Protein was eluted with elution buffer (50 mM sodium phosphate, pH 8.0, 300 mM sodium chloride, 250 mM imidazole) into approximately 1 mL fractions. Fractions were dialyzed against phosphate-buffered saline (1X PBS, 10.9 mM KH_2PO_4, 1550 mM NaCl, 29.7 mM Na_2HPO_4-$7H_2O$, pH 7.4) and analyzed using SDS-PAGE to assess purity.

A 1:10 dilution of the peak fraction of the construct of interest was used to measure the absorbance spectrum and calculate the concentration using Beer's law, where the extinction coefficient of any given construct was 54,000 $(M\ cm)^{-1}$ at 280 nm (21). Absorbance spectra were collected on a Beckman Coulter spectrometer DU800.

2.3 FRET construct cleavage

Eqs. 1.1 and 1.2 require fluorescence measurements of the donor (mCerulean3) in the absence of the acceptor (mCitrine). We do not have access to purified donor alone in our group. Thus, we carried out the following control, which allows us to monitor mCerulean3. We cleave the flexible linker with brief digestion using proteinase K (38). Potential dimerization of fluorophores are minimized, post-digestion, due to the A206K mutation and low concentrations (~500 nM) of protein.

To cleave the construct, we used 0.56 ng of proteinase K per μmol of purified construct and incubated the reaction for 1 min (25°C). To prevent further cleavage and keep our fluorophores intact, we inhibited the reaction with 20 μmol phenylmethylsulfonyl fluoride per mg proteinase K. To ensure the cleavage reaction was successful, we used SDS-PAGE analysis (bands ~30 kDa).

2.4 Heterogeneous and homogenous sample preparation

We prepared stock solutions of Ficoll-70 in 1× PBS (300 g/L) and glycerol in 1× PBS (900 g/L) approximately 24 hours prior to the completion of construct purification. Due to the slow dissolving rate of Ficoll-70, we weighed samples, brought the sample to

approximately 75% volume, allowed the Ficoll-70 to dissolve overnight at rest (4°C). We brought the stock solution to the final volume the following day. On the day of experiments, 250 μL aliquots of various environments, heterogeneous (Ficoll-70, 0–300 g/L) and homogenous (glycerol, 0–760 g/L), were created in 1.5 mL microcentrifuge tubes and briefly vortexed prior to the addition of a construct to ensure an even distribution of molecules.

Immediately prior to fluorescence-based experiments, a construct would be added to each environment. The amount of construct added would depend on the initial concentration, as described in Section 2.2. Typically, construct was added to an approximate concentration of 500 nM.

2.5 Steady-state fluorescence characterization

We carried out steady-state fluorescence measurements on a Jobin Yvon Fluorolog spectrometer FL1039/40. Using 500 nM GE construct in PBS, we optimized excitation and emission slit widths (1.6 nm for both). Samples were prepared as described in Section 2.4 and placed in a 700 μL cuvette with a 1 mL adapter. We used 425 nm for the excitation wavelength, and the emission spectra were collected from 435–600 nm. Once collected, we normalized each trace to the maximum intensity using Origin 8.1 software.

2.6.1 Theory of time-correlated single photon counting (TCSPC)

Time-correlated single photon counting allows for building a probability histogram of detecting a photon as a function of time (44). The high signal-to-noise ratio histogram can then be fit to extract valuable information of the excited-state dynamics. TCSPC also can also be modified to incorporate scanning modes, thereby allowing fluorescence lifetime imaging microscopy (FLIM).

Briefly, a constant fraction discriminator enables us to discriminate the signal from background noise. The time amplitude converter allows for accurate measurement for the arrival time of a laser pulse, which is relayed to the computer using a fast photodiode. The system response function (SRF) was measured to deconvolute the

fluorescence decays to extract a more exact decay. The measured response function underestimates the known lifetimes of our standards, rhodamine 110 and 7-hydroxycoumerin by an estimated 4.8 %. For more analysis on the SRF, please see Section 2.9. Figure 2.1 shows the scheme of our experimental setup.

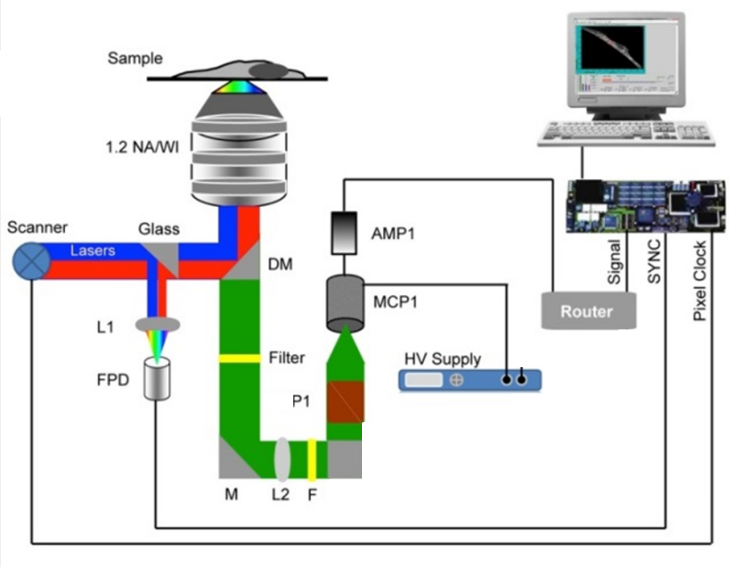

Figure 2.1: Representative diagram of the optical system used for the TCSPC technique used in this Thesis. M: mirror, L:lens, FPD: fast photodiode, NA/WI: numerical aperture/water immersion, DM: dichroic, F: Filter, P1: polarizer, MCP1: microchannel plate, AMP: amplifier.

2.6.2 Optical setup for TCSPC technique and fluorescence lifetimes measurements

For experiments using TCSPC techniques, we use the dichroic mirrors x396rdc and FITC for 425 nm and 465 nm excitation, respectively, and band pass filters 475/50 and 531/40 for detecting donor and acceptor emission, respectively. Laser pulses were generated at 76 MHz, using a titanium-sapphire crystal (Mira 900-F, Coherent). A Russian blue filter was also used to prevent direct laser emission. The average power for the two-photon laser ranged between 480–800 mW, with a pump laser setting of 6.5–7 W, depending on laser wavelength used in the experiment. After being directed to the objective (1.2 NA, Olympus UPlanApo IR, water immersion, 60×), the fluorescence was directed through a magic angle (54.7°) polarizer and onto a microchannel plate photomultiplier tube (R3809U, Hamamatsu). We then collected the respective histograms using SPC-830 software (Becker & Hickl).

2.7 Analysis of TCSPC data

After data collection, we transferred decays from SPC-830 to SPCImage (Becker & Hickl). A complete multi-exponential decay model using a computer-generated system response function was used to fit the data. We fixed the offset based on the background signal-to-noise, while shifting and scattering parameters remained unfixed, due to their minimal effects on the fitting parameters. To determine whether fits were acceptable using a single or biexponential decay (Eq. 2.1), the data from approximately 0.18 to 17.5 ns were fit to both single and biexponential decays. We then compared χ^2 values and the residuals of both fits. We repeated this process for both bi- and triexponential fits as well. After determination of the exponential that best describes the fit, we then extended the range to include the full decay, (approximately –2 to 17.5 ns).

$$F(t) = \sum_i A_i e^{-t/\tau_i} \tag{2.1}$$

2.8 Fluorescence resonance energy transfer theory

The theory behind FRET can be summarized via several equations. Arguably the most important parameter to calculate is the rate, k_{et}, for which energy transfer occurs, as described in Eq. 2.2.

$$k_{et}(r_{da}) = \frac{1}{\tau_D}\left(\frac{R_0}{R_{da}}\right)^6 \tag{2.2}$$

The Förster distance, R_0, is defined as the average donor–acceptor distance at which 50% FRET efficiency occurs. R_0 can be calculated via Eq. 2.3 using steady-state spectroscopy, where κ^2 is assumed to be 2/3 for randomly oriented dipole moments of donor and acceptor (46). We recognize our FRET pair is tethered so this assumption may not be entirely correct, but due to the difficulty of accurate measurements for κ^2, we use this assumption. Q_D is the fluorescence quantum yield of the donor and n is the refractive index of the surrounding environment.

$$R_0^6 = 8.785 \times 10^{-25}\,\frac{\kappa^2 Q_D J(\lambda)}{n^4} \tag{2.3}$$

The spectral overlap, J(λ), is calculated based on steady-state absorbance and fluorescence emission following Eq. 2.4.

$$J(\lambda) = \frac{\int_0^\infty F_D(\lambda)\varepsilon_A(\lambda)\lambda^4\, d\lambda}{\int_0^\infty F_D(\lambda)\, d\lambda} \tag{2.4}$$

Because our linker is flexible we expected that the distance between the fluorophores change in various environments. Therefore, it is difficult to use the above equations to calculate the k_{et} for our systems of interest. A more practical way to measure FRET efficiency has been developed using Eqs. 2.5 and 2.6 for steady-state and time-resolved fluorescence intensities where F_{DA} and τ_{DA} are the respective intensity and average lifetime of the donor in the presence of acceptor, and F_D and τ_D are the respective intensity and average lifetime of the donor alone.

$$E(\%) = 100\left(1 - \frac{F_{DA}}{F_D}\right) \tag{2.5}$$

$$E(\%) = 100\left(1 - \frac{\tau_{DA}}{\tau_D}\right) \tag{2.6}$$

We can then use the time-resolved fluorescence lifetime measurements to estimate k_{et} using Eq. 2.7 (46).

$$E = \frac{k_{et}}{(\tau_D)^{-1} + k_{et}} \tag{2.7}$$

Finally, if we can calculate the Förster distance from steady-state spectroscopy, we can then combine the lifetime results to calculate the average physical distance between our donor and acceptor fluorophores. This relationship is described in Eq. 2.8 and Figure 2.2. Based on this relationship, donor–acceptor distances closest to the Förster distance should induce the greatest changes in FRET efficiency.

$$E = \frac{R_0^6}{R_0^6 + R_{da}^6} \tag{2.8}$$

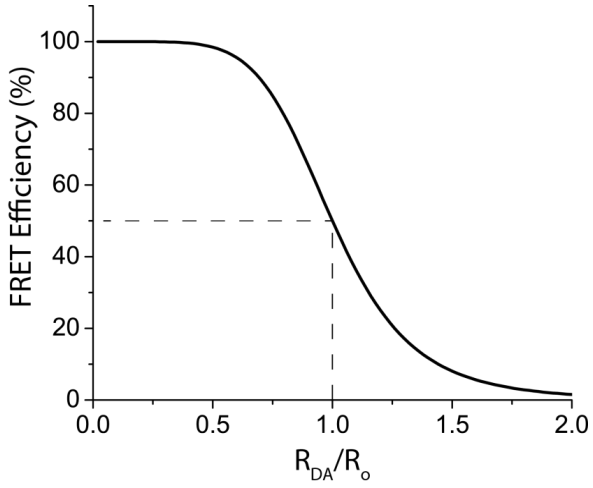

Figure 2.2 The theoretical relationship between the donor–acceptor distance of a FRET pair and FRET efficiency.

Table 2.1 Standards measured via TCSPC at various excitations and detections to determine best method of fitting.

$\lambda_{excite} - \lambda_{detect}$:	**Lifetime Measured SRF (ns)**	χ^2 **Measured SRF**	**Lifetime CPU Generated SRF (ns)**	χ^2 **CPU Generated SRF**
rhodamine 110 465–531/40 nm	3.81	1.30	4.00	1.41
rhodamine 110 425–531/40 nm	3.85	1.23	4.01	1.38
7-hydroxylcoumarin 425–475/50 nm	3.88	1.11	4.00	1.26

Section 2.9 Instrument response function and computer-generated response function

We measured our response function using the same optical setup as described in Section 2.6.2. We used 2% milk as the scattering solution and detected a small amount of photons directly from the laser. The measured system response function is shown in Figure 2.3. We determined the full-width half maximum to be 59.2 ps.

Upon fitting our standards using our system response function, we estimate the fluorescence lifetime of rhodamine 110 and 7-hydroxylcoumerin to be 3.83 ns and 3.88 ns, respectively. These results compare with the fit using the computer generated response function, 4.00 ns and 4.00 ns, for rhodamine and7-hydroxylcoumerin, respectively. The difference between the fits using either the computer generated response function or measured response function is greater than the known uncertainty of

our measurements (0.03 ns). It should also be noted other studies using rhodamine 110 and 7-hydroxylcoumerin have reported fluorescence lifetimes of 4.00 ns and 4.06 ns, respectively (48, 49). Table 2.1 shows the fitting parameters using both measured and computer-generated response functions. In Table 2.1, one can see the measured response function produces a better fit based on the values of χ^2. Although, it is accepted that the measured response function may lead to more accurate results; due to the newness of the measured response function, along with a slight discrepancy with literature values, the lifetime measurements presented in this Thesis, were fit using a computer generated response function.

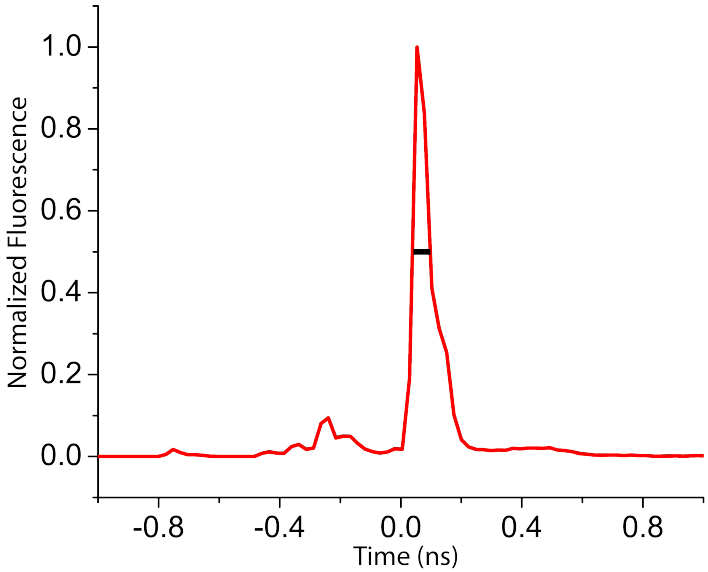

Figure 2.2 The system response function was measured under the experimental conditions as described in section 2.6.2. With a FWHM of 59.2 ps, we estimate the uncertainty to be 20 ps for each measurement when decays are fit to the measured system response function.

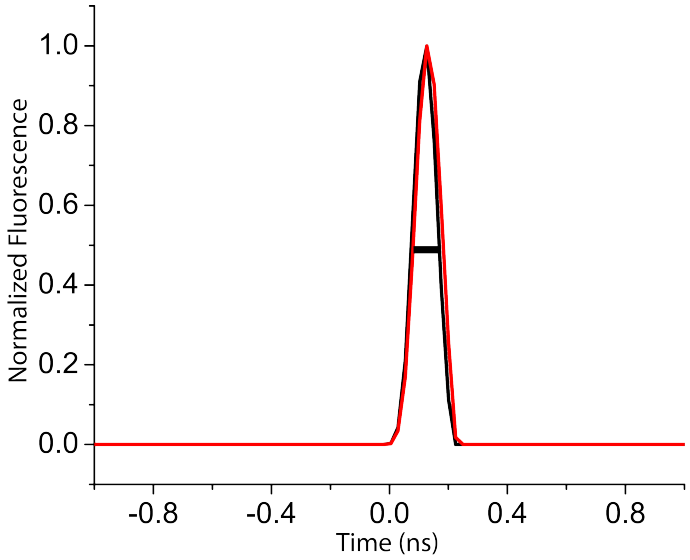

Figure 2.3 Computer generated response functions were produced by SPCImage based on the build-up of fluorescence for 7-hydroxylcoumarin (black) and rhodamine 110 (red). With an average FWHM of 98.5 we estimate the uncertainty per measurment to be 30 ps when decays are fit to the computer generated response function.

Chapter 3
Steady-state fluorescence of the GE construct

Disclosure: This Chapter has been published, in part, in the following:

Currie, M., Leopold, H., Schwarz, J., Boersma, A., Sheets, E.D., Heikal, A.A. (2017) "Fluorescence Dynamics of a FRET Probe Designed for Crowding Studies" *Journal of Physical Chemistry (B).*

This Chapter describes the steady-state spectroscopy collected for the GE probe in heterogeneous and homogenous environments.

3.1 Background

When investigating excited-state dynamics, the steady-state absorbance and fluorescence spectra are vital when it comes to designing the experimental plan. Without these spectra, it is nearly impossible to ensure accurate excitation and detection of the fluorophores involved. Specifically, in our investigations, due to the presence of two fluorophores (mCerulean and mCitrine) in our sensor, it is essential to understand exactly what is being excited and detected. Previous studies have already characterized our probes using steady-state spectroscopy (21, 38), and here we aimed to replicate these results to ensure accurate probe purification and experimental design for our subsequent investigations. These measurements were carried out prior to optimizing the cleavage of the protein constructs; therefore, the observations presented in this Chapter are only qualitative with respect to FRET efficiency.

3.2 Results and discussion

Using the steady-state absorbance of the original protein construct, GE, in PBS (Figure 3.1), we confirmed a maximum absorbance for mCerulean3 and mCitrine, at 433 nm and 514 nm, respectively. However, for our experimental design purposes, we must excite the donor directly and minimize direct excitation of the acceptor. For this reason, we used an excitation wavelength of 425 nm because the absorption for mCerulean3 appears to be an estimated 99% larger than the mCitrine.

We measured the steady-state fluorescence for the range 435–600 nm using 425 nm excitation as a function of the concentrations of heterogeneous crowder (0–300 g/L Ficoll-70) and homogenous crowder (0–900 g/L glycerol) (Figure 3.2). We attribute the qualitative increase of mCitrine's emission (500–550 nm) as [Ficoll-70] increases to higher FRET efficiencies in crowded environments, which is consistent with previous studies (21). Interestingly, upon addition of a homogenous crowder, a slight decrease in the fluorescence contribution of mCitrine is observed, indicating a possible reduction in FRET efficiency; however, previous studies have reported glycerol not having any effect on FRET efficiency (21).

Although our measurements of FRET efficiency are qualitative, we can still use the theory presented in Section 2.7 to calculate R_o for comparison with previous studies. Using the absorbance and emission spectra of the GE protein in buffer, we estimate the spectral overlap to be 1.35×10^{15} M^{-1} cm^3 nm^4. We can then use the quantum yield of mCerulean3, 0.87 (40) and the refractive index of PBS (1.333) to calculate the R_o value of this FRET pair to be 5.3 ± 0.7 nm, which is in reasonable agreement with previously reported R_o value of 5.4 nm (38). Additionally, we used these data to calculate R_o for crowded environments (Table 6.1), which required the refractive indices of experimental conditions (see Appendix B). A further discussion of the Förster distance calculations in crowding solutions is found in Chapter 6.

With this data in hand, we are able to properly design our time-resolved fluorescence lifetime experiments. By exciting at 425 nm we will be able to exclusively excite the donor, while at 465 nm (the highest possible laser line available for our set-up), we will excite both mCerulean3 and mCitrine in relatively equal amounts. We will also be able to detect exclusively mCerulean3 with a 475/50 nm filter, and detect primarily mCitrine with a 531/40 filter. However, before exploring time-resolved lifetime experiments, there is still a need for a kinetic model to describe the fluorescence of our probes. This is discussed in Chapter 4.

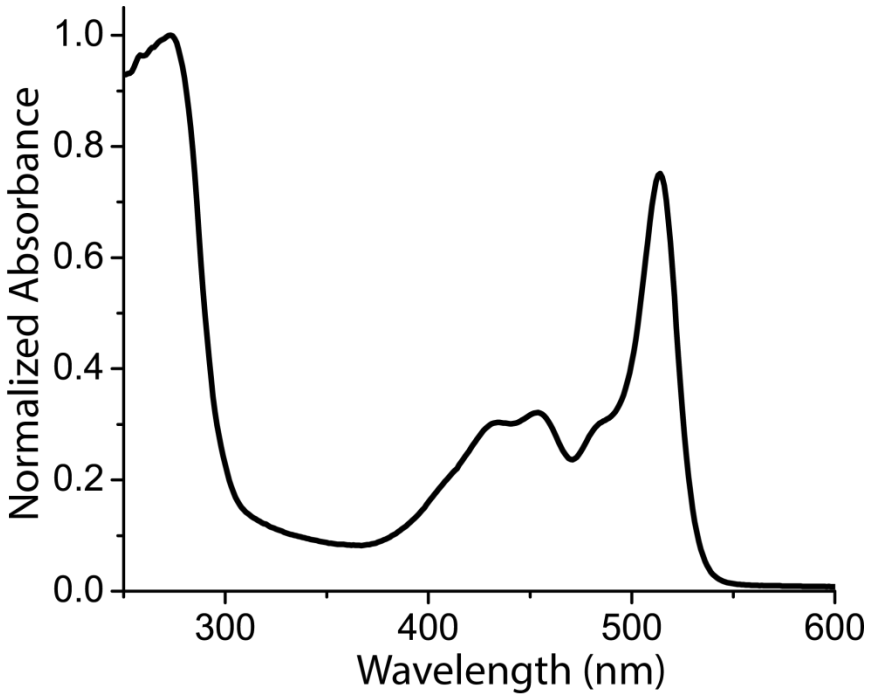

Figure 3.1: Normalized steady-state absorbance of the GE probe in PBS (~12 μM) mCerulean3 (donor) absorbs in the range of 380–500 nm, whereas mCitrine (acceptor) absorbs in the range 455–545 nm.

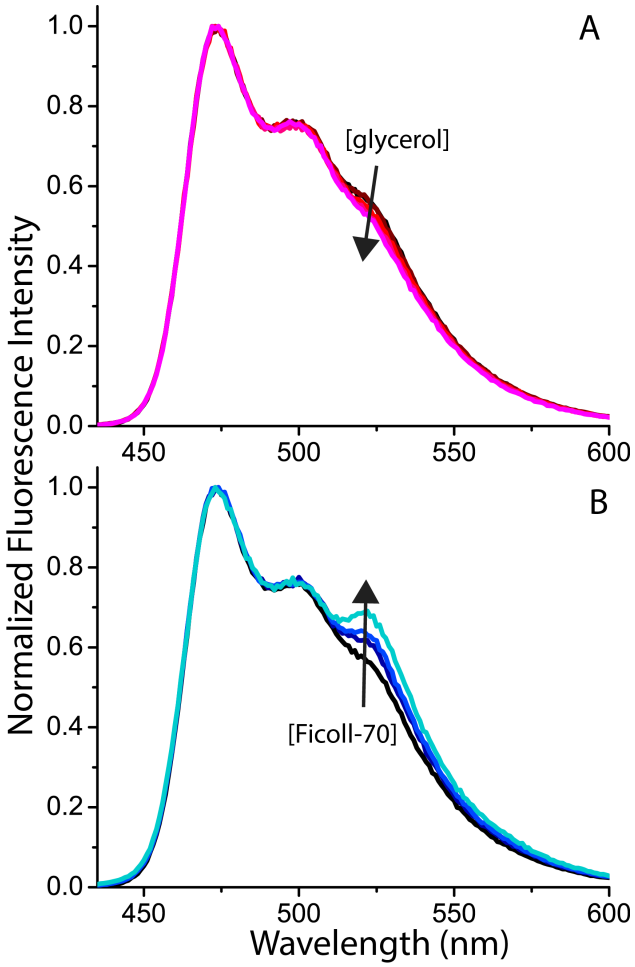

Figure 3.2: Steady-state fluorescence emission spectra of the GE construct in increasing glycerol concentration (Panel A) and Ficoll-70 (Panel B).

Chapter 4:
Kinetic model of excited-state dynamics of FRET constructs using 425 nm excitation and detection

Due to the newness of these probes, there is not yet a kinetic model to describe the excited-state dynamics of these proteins. In this Chapter, we discuss and model the possible scenarios of exciting the donor (425 nm) and detecting the donor (475/50 nm) needed to calculate the FRET efficiency from the well-established theory mentioned in Section 2.6. In Chapter 5 of this Thesis, we will show that the combination of 425 nm excitation and 475/50 nm detection is determined to be the best combination for estimating FRET efficiency. Once we have accounted for all possible scenarios for 425 nm excitation and 475/50 nm detection, we will then use experimental data to determine whether our kinetic model is applicable to our experimental system.

4.1 Modeling 425 nm Excitation and 475/50 nm detection

Consider Figure 4.1 where the molecule D, represents the donor of the FRET sensor, mCerulean3, and the molecule A, represents the acceptor, mCitrine. When exciting at 425 nm, we only excite the donor molecule because the absorbance for the donor is an estimated 99% greater than the acceptor at the same wavelength (Figure 3.1). For detection, we use a 475/50 nm emission filter, which blocks an estimated 99% of photons from the acceptor. This experimental setup results in the following scenarios, which are shown in Figure 4.1: Scenario 1: the population of excited constructs is incapable of FRET; Scenario 2: the population of excited constructs is capable of FRET; and finally Scenario 3: there are two unique populations, one capable of undergoing FRET and the other incapable of FRET.

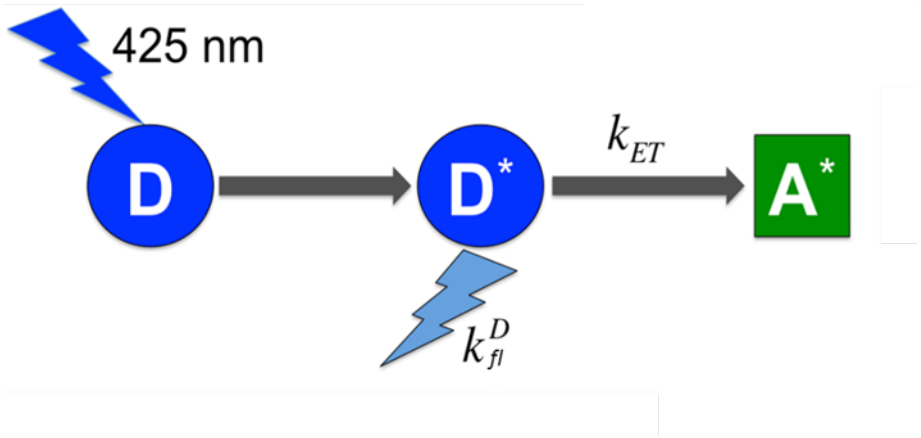

Figure 4.1 A diagram on all possible energy pathways under 425 nm excitation and 475/50 nm detection.

For Scenario 1, we can describe an excited donor molecule incapable of FRET ($k_{et} = 0$) via the following equation, where

$$dN_1 = -\left(k_{fl}^{D}\right)N_1 \tag{4.1}$$

This differential has the solution of:

$$N_1(t) = N_1 e^{-(k_{fl}^{D})t} \tag{4.2}$$

For Scenario 2, we describe the population of excited donor molecules capable of going through FRET as decaying via the equation:

$$\frac{dN_2}{dt} = -(k_{fl}^{D} + k_{et})N_2 \tag{4.3}$$

This differential then has the solution of:

$$N_2(t) = N_2 e^{-(k_{fl}^{D}+k_{et})t} \tag{4.4}$$

For Scenario 3, we model two populations, one capable of FRET and the other incapable of FRET. Accounting for the entire ensemble of probes, we can simply add the two populations, described in Eqs. 4.1 and 4.3, to describe the total decay as follows:

$$\frac{dN_{total}}{dt} = -(k_{fl}^{D})N_1 - (k_{fl}^{D} + k_{et})N_2 \tag{4.5}$$

Having already solved for these decays, we substitute Eqs. 4.2 and 4.4 to derive the final solution:

$$N_{total}(t) = N_1 e^{-(k_{fl}^{D})t} - N_2 e^{-(k_{fl}^{D}+k_{et})t} \tag{4.6}$$

Using this equation, we also notice that the k_{et} presented in this equation will over estimate energy transfer, for the entire ensemble, as it is only characteristic of one population. Therefore, we have altered equation 2.7 to correct for this overestimation as follows:

$$E_{total}(\%) = 100\left(\frac{k_{et}}{\tau_D^{-1} + k_{et}}\right)\left(\frac{N_2}{N_1 + N_2}\right) \tag{4.7}$$

4.2 Simulation of model

Figure 4.2 shows simulations for Scenarios 2 and 3 described above undergoing 425 nm excitation and 475/50 nm detection. These simulations allowed us to predict the fluorescent decays as a function of energy transfer. Using the Eqs. 4.4 and 4.6, we use the k_{et} range of 0.125–4 ns^{-1}. This range was chosen as our earlier experiments estimate these probes to have a range of k_{et} of 0.2—0.8 ns^{-1}. The single exponential decay model (Scenario 2) assumes all probes are capable of FRET, and the decay is affected considerably by changes in energy transfer rates. Meanwhile for the biexponential model (Scenario 3) we fixed the populations (50% capable of FRET and 50% incapable of FRET). The inclusion of distinct populations drastically changes the shape of the curve, as shown in Figure 4.2.

4.3 Discussion of model: does the modeling agree with experimental results?

Table 4.1 describes the fitting parameters of five constructs in buffer fit in the absence of the model. Most importantly, the intact probes decay as a biexponential decay, therefore the first two scenarios are invalid for our intact systems. However, revisiting the first scenario, we make the assumption that the cleaved constructs are incapable of FRET, and therefore can be modeled via Eq. 4.2. This model for the cleaved constructs is in line with experimental data (Figure 5.1A). Importantly, it is also known that the donor, mCerulean3, was genetically modified to fluoresce as a single-exponential (40), this is also in agreement without model.

For the modeling of intact probe, we used the simulations presented in Section 4.1. In Table 4.2 we see the experimental fitting parameters of intact probes undergoing 425 nm excitation and 475/50 detections, due to the biexponetial nature of these fits, it was determined scenario 3 described in section 4.1 best agrees with our experimental results. This agreement is also based on the shape of the decay curve as a function of k_{et} in both simulation (Figure 4.2B) and experimental results (Figure 5.2A). As we describe in Chapter 5, we observe that all five constructs behave similarly to the model with unique biexponential decay constants (Figure 5.2A). The simulation (Figure 4.2B) and experimental results (Figure 5.2A) have similar distortion in shape when increasing k_{et}. Differences between the experimental results and the simulations can be attributed to the variation of populations because the simulation was carried out with fixed population ratios, whereas, as discussed in Chapter 6, these populations may be dynamic and change as a function of specific environment.

We then further explored the model in Scenario 3. Upon derivation of this model, we reanalyzed intact constructs. We fixed one exponential term to the lifetime of the cleaved constructs, but both pre-exponential factors and the second exponential term were allowed to be fit. The reanalysis is shown in Table 4.2. Comparing Table 4.1 and 4.2 we see, GE, E6G2, and E6 obtain smaller χ^2 values when using the model, and

although the χ^2 values for G18 and G12 rose, the residual plot remained consistent. Additionally, the energy transfer efficiency is still in reasonable agreement in both fitting Scenarios. For these reasons, all data shown shown in Chapters 5 and 6 are fit using Eq. 4.6 and Eq. 4.2 for intact and cleaved constructs, respectively.

It is also important to note that the fluorescence lifetime decays measure the amount of time a molecule spends in the excited state, k_{fl}, which is a combination of radiative and non-radiative processes as described by Eq. 4.8.

$$k_{fl} = k_{rad} + k_{non-rad} \tag{4.8}$$

Using TCSPC, we can directly measure k_{fl} of a given system. Changes in k_{rad} can be predicted using the Strickler-Berg equation Eq. 4.9 (47). Because the fluorophores, mCerulean and mCitrine, are identical in each of our constructs, we can simplify the Strickler-Berg equation as follows:

$$k_{rad} = 2.88x10^{-9} n^2 \frac{\int_{\Delta\nu_f} F(\bar{\nu})d\nu}{\int_{\Delta\nu_a} F(\bar{\nu})\nu^{-3}d\nu} \int_{\Delta\nu_a} \zeta(\bar{\nu})d\ln\bar{\nu} \tag{4.9}$$

$$k_{rad} = cn^2 \tag{4.10}$$

Substituting equation 4.9 into equation 4.8 gives us:

$$k_{fl} = cn^2 + k_{non-rad} \tag{4.11}$$

Eq. 4.10 is plotted in Figure 4.3 for the representative E6G2 construct. It is important to note that FRET is a non-radiative process. Therefore, according to equation 4.11, deviation from equation 4.10 will indicate a change in non-radiative processes, e.g. FRET efficiency. Cleaved versions of our constructs follow the Strickler-Berg equation, regardless of the environment (Figure 4.3A), this indicates there is no change in $k_{non-rad}$ and therefore FRET efficiency. In homogenous environments, intact constructs also follow the Strickler-Berg equation. However, when examining intact probe in Ficoll-70

enriched environments, we observe that one component agrees with Eq. 4.10 and the other component deviates drastically. In Chapter 3, we established FRET efficiency increases upon heterogeneous environments. If Eq 4.6 is correct, for heterogeneous environments, we would observe one component following the Strickler-Berg relationship and one component deviating, which is exactly what we observe in Figure 4.3B. Full fitting parameters and FRET efficiencies are given in Table 4.3.

4.4 Conclusions

The model for Scenario 1 describes a system where no FRET occurs and is therefore analogous to our cleaved probes. Because mCerulean3 decays as a single exponential (39), the model is in reasonable agreement our experimental results shown in Figure 5.1A . Using the model for Scenario 1, we can directly measure rate of fluorescence of the donor alone, k_{fl}^{d}.

The biexponential model described as Scenario 3 best agrees with our intact probes experimental data shown in part in Tables 4.1 and 4.2. Given these results, we decided to fit our experimental results using this scenario. By directly measuring k_{fl}^{d} first, we are able to assign one of the exponential terms to that of the donor alone. Scenario 3 also suggests there are two distinct populations, one capable of undergoing FRET and the other incapable of undergoing FRET. This scenario is slightly counterintuitive because the fluorophores are linked, which keeps the donor–acceptor distance small. However, in combination of the simulation results agreeing with the decays shown in Chapter 5, and results of the Strickler-Berg relationship, there are clearly two populations present.

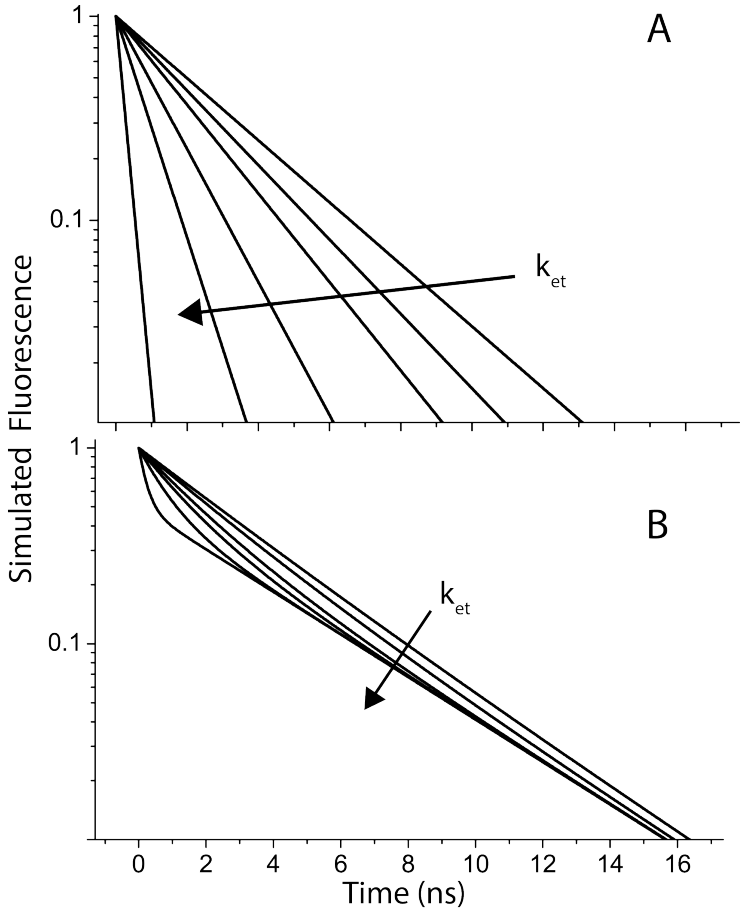

Figure 4.2 Simulated fluorescence decays based on the modeling of Eqs. 4.4 (Panel A) and 4.6 (Panel B). These simulations are for the k_{et} range of 0.125–4 ns.

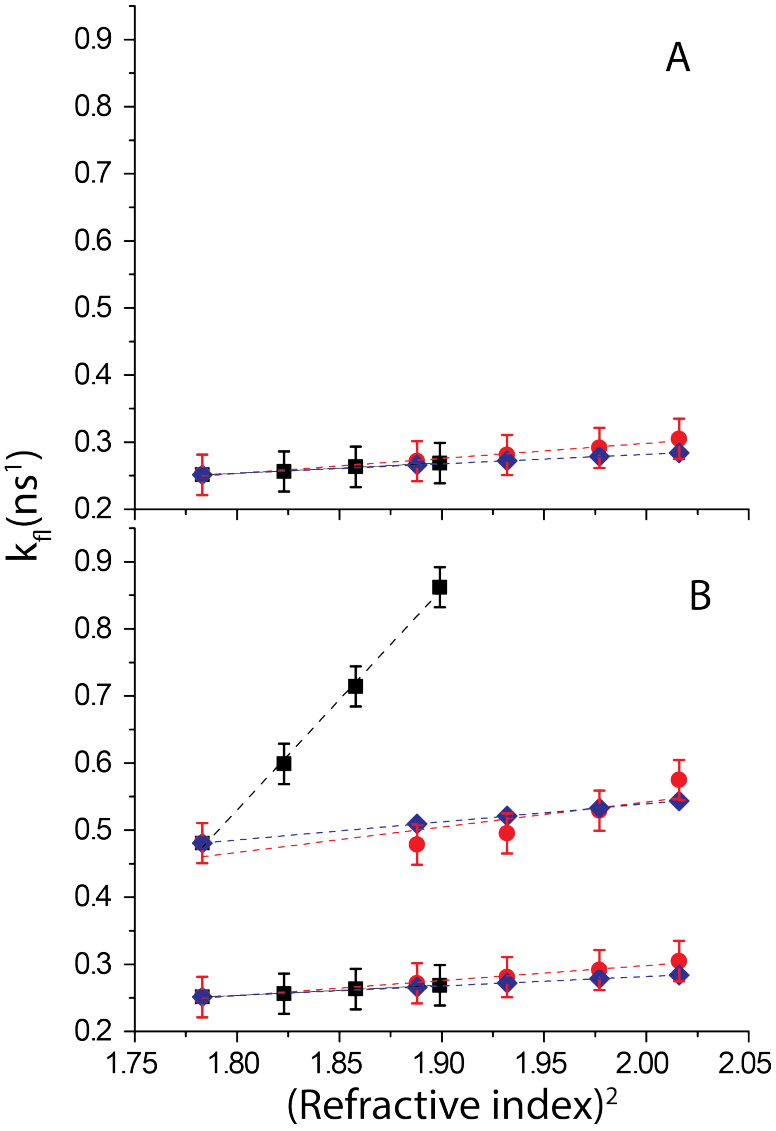

Figure 4.3 The fitting parameters for cleaved (Panel A) and intact (Panel B) E6G2 construct in both Ficoll-70 (0–300 g/L) (black squares) and glycerol (0–760 g/L) (red circles). Additionally, a modified Strickler-Berg equation (Eq. 4.10) was also plotted (blue diamonds). Error based on 20% the FWHM of the system response function. The dotted line is for visual guidance for trend and not a fit.

Table 4.1 Fluorescence lifetime decays of fitting parameters collected via TCSPC of intact constructs in PBS and energy transfer rates based on Eq. 2.6 in the absence of derived model. Decays collected using 425 nm excitation and 475/50 nm detection. Error based on 20% the FWHM of the system response function.

Construct	A_1 (%)	τ_1 (ns)	A_2 (%)	τ_2 (ns)	$\langle\tau\rangle$ (ns)	χ^2	E (%)
GE	71.8	3.27 ± 0.03	28.2	4.85 ± 0.03	3.72 ± 0.03	1.37	6.77 ± 0.6
E6G2	67.4	3.05 ± 0.03	32.6	4.75 ± 0.03	3.61 ± 0.03	1.33	9.52 ± 0.6
E6	65.2	2.94 ± 0.03	34.8	4.68 ± 0.03	3.54 ± 0.03	1.32	12.2 ± 0.6
G18	54.1	2.27 ± 0.03	45.9	4.17 ± 0.03	3.14 ± 0.03	1.16	20.9 ± 0.7
G12	36.8	1.55 ± 0.03	63.2	3.80 ± 0.03	2.97 ± 0.03	1.12	25 ± 1

Table 4.2 Fluorescence lifetime decay fitting parameters collected via TCSPC of intact constructs in PBS, using the model described in Section 4.3.3. Decays collected under 425 nm excitation and 475/50 nm detection. Error based on 20% the FWHM of the system response function.

Construct	A_1 (%)	τ_1 (ns)	A_2 (%)	τ_2 (ns)	$\langle\tau\rangle$ (ns)	χ^2	E (%)
GE	16.4	2.14 ± 0.03	83.6	3.99 ± 0.03	3.69 ± 0.03	1.32	7.52 ± 0.6
E6G2	22.1	2.06 ± 0.03	78.0	3.99 ± 0.03	3.56 ± 0.03	1.21	12.2 ± 0.6
E6	24.7	2.00 ± 0.03	75.3	3.98 ± 0.03	3.45 ± 0.03	1.22	13.3 ± 0.6
G18	40.3	1.78 ± 0.03	59.7	3.97 ± 0.03	3.09 ± 0.03	1.35	22.2 ± 0.7
G12	44.6	1.80 ± 0.03	55.4	3.98 ± 0.03	3.01 ± 0.03	1.62	24 ± 1

Table 4.3 Squared refractive index and fitted rate constants of biexponential decays of the E6G2 construct in various crowded environments. We calculated the change in k_{rad} constant via Eq. 4.10. Error based on 20% the FWHM of the system response function.

Environment	Refractive Index^2	$k_1(ns)^{-1}$	$k_2(ns)^{-1}$	k_{rad1} $(ns)^{-1}$	k_{rad2} $(ns)^{-1}$	E (%)
PBS	1.783	0.481 ± 0.03	0.251 ± 0.03	0.481	0.251	12.2 ± 0.6
Ficoll-70 100 g/L	1.823	0.599 ± 0.03	0.256 ± 0.03	—	—	15.4 ± 0.7
Ficoll-70 200 g/L	1.858	0.714 ± 0.03	0.263 ± 0.03	—	—	18.1 ± 0.8
Ficoll-70 300 g/L	1.899	0.862 ± 0.03	0.269 ± 0.03	—	—	21.8 ± 0.8
Glycerol 340 g/L	1.888	0.478 ± 0.03	0.272 ± 0.03	0.509	0.266	8.97 ± 0.7
Glycerol 480 g/L	1.932	0.495 ± 0.03	0.281 ± 0.03	0.521	0.272	8.71 ± 0.7
Glycerol 620 g/L	1.977	0.529 ± 0.03	0.292 ± 0.03	0.533	0.279	9.04 ± 0.8
Glycerol 760 g/L	2.016	0.575 ± 0.03	0.305 ± 0.03	0.544	0.284	9.76 ± 0.8

Chapter 5:

Characterization of novel sensors in PBS: wavelength-dependence and effects of linker length and structure

Disclosure: This Chapter has been published, in part, in the following:
Currie, M., Leopold, H., Schwarz, J., Boersma, A., Sheets, E.D., Heikal, A.A. (2017) "Fluorescence Dynamics of a FRET Probe Designed for Crowding Studies" *Journal of Physical Chemistry (B).*

This Chapter describes the characterization of wave-length dependence of these probes undergoing excitations of either 425 nm or 465 nm and detection of either 475/50 nm or 531/40. The constructs linkers, lengths and structures were measured in PBS buffer.

5.1 Background

By characterizing the five constructs, in phosphate-buffered saline, we gain knowledge into their behavior and better understand the importance of linker, length and structure. In this Chapter, we investigate wavelength dependence as well as differences in linker, length and structure for all five probes. Due to the presence of mCerulean and mCitrine within these probes, it was critical to determine whether there is a wavelength dependence upon either excitation and/or detection. By varying the excitation and detection wavelengths, we aimed to determine the ideal scenario for estimating FRET efficiency. Once the ideal scenario to estimate FRET efficiency was determined, we then characterized the effects of the linker in the controlled environment of PBS. To distinguish between the effects of length and structure, we compared two constructs at a time, G18 to G12, and E6 to E6G2, for linker, length and structure effects respectively. We chose the G18 and G12 constructs to compare length due to identical structure within the linker region as the only difference between the constructs is the number of loop repeats $(–GSG–)_n$ and therefore only differ in length. Meanwhile E6 and E6G2 contain the same number of amino acids but differ in the ratio (m/n) of rigid helical repeats $(–EAAAK–)_m$ to flexible loop repeats $(–GSG–)_n$. E6G2 has a much more rigid linker with a

helix/loop ratio of 6.0 compared to the ratio of E6 at 0.5 (38). We also investigate the effects of the linker length on the cleaved FRET probe as a control.

5.2.1 Characterization of excited-state wave-length dependence

Looking first at the cleaved constructs we see similar decays between all of the constructs no matter the excitation or detection wavelengths (Figure 5.1). These similar decays are most likely due to all of the constructs containing the same fluorophores (mCerulean3 and mCitrine) which only differ in linker. In other words, upon cleavage of the linker, the samples are expected to become negligibly different. This expectation was confirmed, as shown in Figure 5.1. Additionally, when we excite with either 425 nm or 465 nm, we observe faster lifetimes using 531/40 nm detection (Figure 5.1B-C) detection as compared to 475/50 nm detection (Figure 5.1A). These results suggest that mCitrine may have a shorter lifetime, than mCerulean3. These results are in general agreement with previous studies, which have found the lifetime of mCitrine as 3.61 ns (50) and mCerulean3 4.0 ns (39).

In contrast, when we measure the fluorescence lifetimes of the intact protein constructs, under 425 nm excitation and 475/50 nm detection (Figure 5.2A), we observe that each construct displays a unique fluorescence decay. These unique decays appear to differ based on the rate of energy transfer and can therefore be used to estimate energy transfer efficiency. However, because changes in refractive index have an impact on the decays, we also need to use the decays of cleaved constructs, under similar conditions (environment, excitation, and detection) to accurately estimate energy transfer efficiency. By comparing the lifetime of the donor alone with the lifetime of intact probe, given both are measured in the same environment, we can account for changes in refractive index.

Interestingly, when detecting the acceptor for intact probes, we again see little difference in the fluorescence lifetime decays, for both 425 nm and 465 nm excitation (Figure 5.3B,C). These indistinguishable decays make estimating energy transfer challenging. Therefore, we used the ideal experimental combination of 425 nm excitation and 475/50 nm detection to estimate FRET efficiencies.

5.2.2 Characterization of linker, structure and length

The distinct lifetime decays of the intact constructs under 425 nm excitation and 475/50 nm detection allow us to calculate FRET efficiency, following Eq. 4.7. This calculation assumes that the lifetimes of the cleaved probes' mCerulean can be used as the lifetimes of the donors (mCerulean in the intact protein) alone. When we compare comparing the proteins G12 and G18 (Figure 5.3), we observe that the shorter linker length results in a high FRET efficiency, as we would expect based on these proteins having flexible and short linkers. It is surprising though that this increase in FRET efficiency is not even larger (24.4% for G12 as compared with 22.2% for G18; Table 4.2), given that the linker length of G12 is approximately one-third the length of that of G18.

Interestingly, the rigidity of the linker's structure also has a direct effect on FRET efficiency. As shown in Figure 5.3 by comparing E6G2 and E6, we observe that the more rigid E6G2 has lower FRET efficiency (12.2%; Table 4.2) than that of the more flexible E6 (13.3%; Table 4.2) despite having similar linker lengths. We hypothesize that the rigid α-helices in the E6G2 protein act to keep the fluorophores farther apart, in contrast to the more flexible region of the E6 that is able to take on a more compact conformation thereby resulting in greater FRET efficiency. This conformational change may also explain the surprisingly little change in FRET efficiency between the more flexible G12 and G18, despite their respective linker lengths as mentioned above. It appears the flexible loop regions of these constructs may likely be able to become more compact, even in the absence of crowding.

5.3 Conclusions

By varying the excitation and detection wavelengths, we have demonstrated that there is a wavelength dependence when investigating these probes. Importantly, only one of these excitation and detection combinations results in unique lifetime decays and allows for accurate estimation of FRET efficiencies: that is, 425 nm excitation and 475/50 nm detection. Using these excitation and detection wavelengths, we calculated the FRET efficiencies for the controlled environment of PBS (Table 4.2). These findings

allow us to compare the effects of both the length and rigidity of the linkers of these protein constructs. Perhaps not surprisingly, the shorter linker lengths have increased FRET efficiencies, which we attribute to shorter donor-acceptor distances. Additionally, our results also show that constructs with greater loop/helix ratios are more flexible and may also lead to shorter donor-acceptor distances by taking on more compact conformations regardless of crowding concentrations.

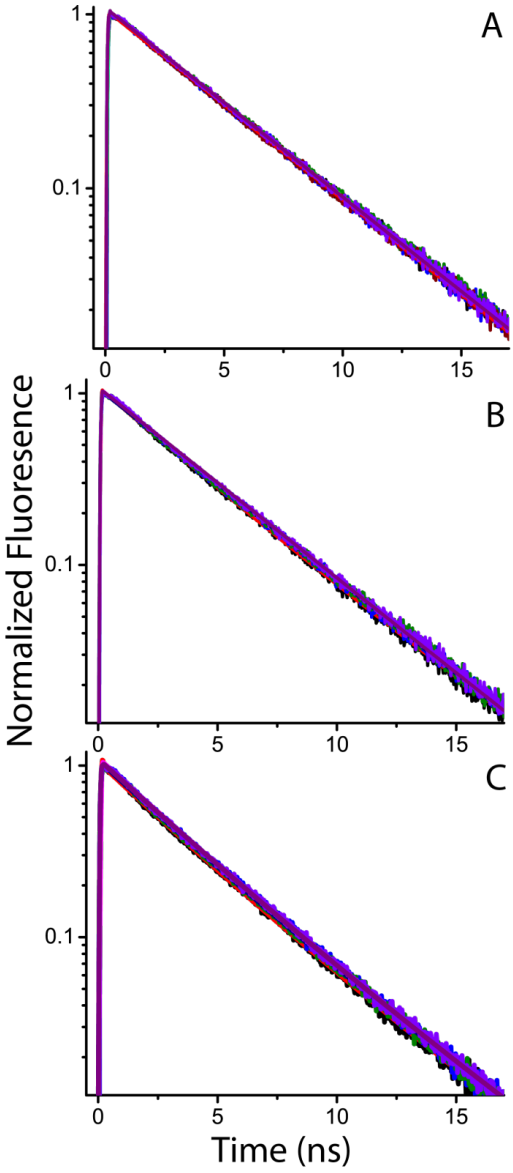

Figure 5.1 Time-resolved fluorescence decays of all cleaved constructs in PBS. 425 nm excitation and 475/50 nm detection (Panel A) shows the longest lifetime because the donor has a longer lifetime than the lifetime of the acceptor. Meanwhile, 425 nm and 465 nm excitation with 531/40 nm detection (Panels B and C, respectively) results in the shorter lifetimes as the 531/40 nm filter primarily detects the fluorescence of mCitrine.

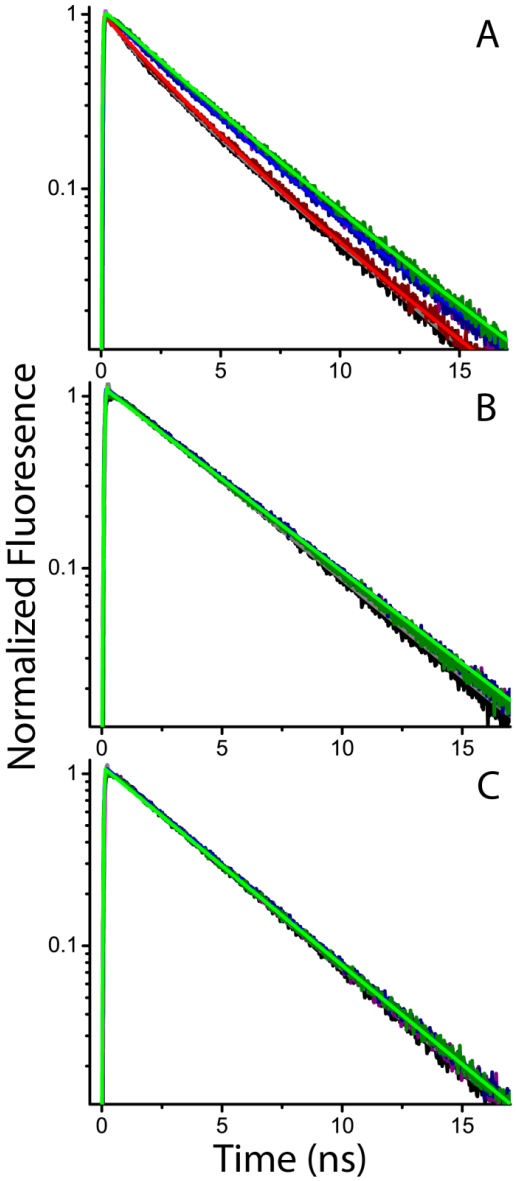

Figure 5.2 Fluorescence decays of intact probes GE (green), E6G2(pink), E6 (blue), G18 (red) and G12 (black) in PBS under 425 nm excitation and 475/50 nm detection (Panel A), 425nm and 465 nm excitation with 531/40 nm detection (Panels B and C respectively).

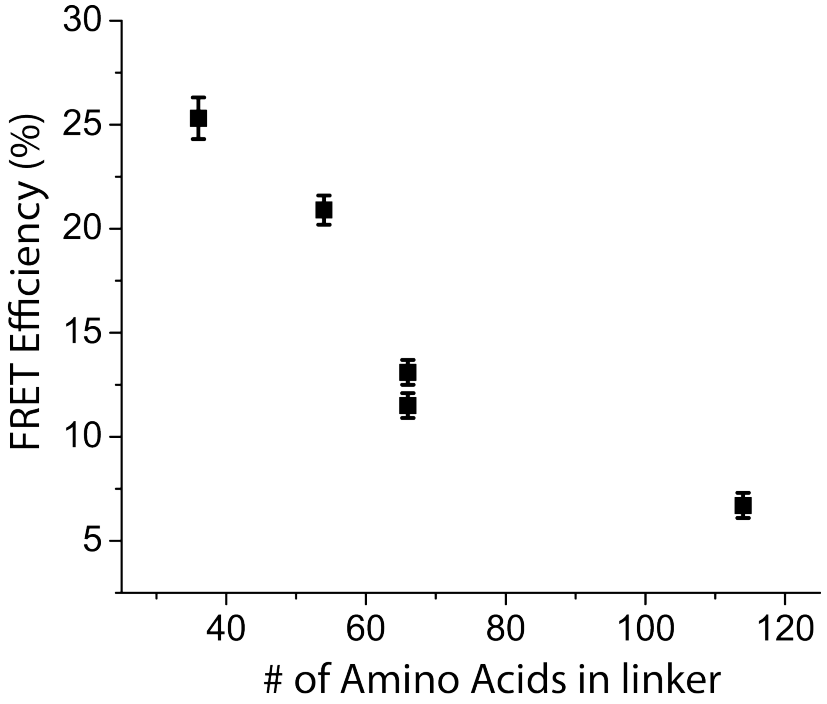

Figure 5.3 FRET efficiencies of each construct in PBS calculated using Eq. 4.7. We assume the average lifetime of the cleaved constructs is equal to the lifetime of the donor alone.

Chapter 6
Characterization of novel sensors as a function of heterogeneous crowding concentration (Ficoll-70) and homogenous crowding (glycerol)

Disclosure: This Chapter has been published, in part, in the following:
Currie, M., Leopold, H., Schwarz, J., Boersma, A., Sheets, E.D., Heikal, A.A. (2017) "Fluorescence Dynamics of a FRET Probe Designed for Crowding Studies" *Journal of Physical Chemistry (B)*.

This Chapter describes the characterization of the conformational changes of all constructs in heterogeneous and homogenous environments.

6.1 Background

The aim of this Chapter was to directly test the hypotheses that these FRET probes will undergo conformational changes in the presence of macromolecular crowding to favor more compact conformations, thereby leading to enhanced FRET efficiencies. We also hypothesize that the conformations of these probes will be independent in homogeneous, highly viscous environments. By using the model discussed in Chapter 4 and methods in Chapter 2, we measured both intact and cleaved decays in various concentrations of heterogeneous crowder (Ficoll-70) and homogenous viscosity (glycerol). We chose the concentration gradient for Ficoll-70, 0–300 g/L, to mimic crowding concentrations in living cells (2) as discussed in Section 1.2. Meanwhile, the glycerol concentration, 0–760 g/L, was varied to control for the bulk viscosity and refractive index changes induced by high concentrations of Ficoll-70. We also controlled for the refractive index (discussed in Section 2.6) by measuring the cleaved probe in each environment (buffer, glycerol-enriched buffer, Ficoll-70 enriched buffer) for refractive index changes across the concentration ranges. Using this information, we were able to calculate the FRET efficiencies using Eq. 4.7.

6.2.1 FRET efficiencies calculated using 425 nm excitation (donor) and 475/50 nm emission.

In this project, we aimed to determine which of these probes will behave most ideally for future *in vivo* studies. Figure 6.1 shows that E6G2 and E6 appear to be the most sensitive to heterogeneous crowding, as indicated by the largest range in the FRET efficiency differences, 9.4% and 5.9% respectively. Although all of the constructs are observed to increase their FRET efficiency upon heterogeneous crowding, we also observe a trend of decreasing FRET efficiency as the viscosities of glycerol-enriched buffer increases. G12 was the most sensitive the higher glycerol concentration, with an estimated decrease of 5.5% in the range of FRET efficiency differences.

These results seem to support our hypothesis with respect to the behavior of the FRET sensors in heterogeneous environments. However, the decrease in FRET efficiency in the homogenously viscous environments would appear to contradict our hypothesis that viscosity alone would not affect the FRET efficiencies of these proteins. To further investigate the quandary, we investigated the donor–acceptor distances.

Although FRET efficiency is directly related to donor–acceptor distance, it is also critical to account for changes in refractive index that result from these high concentrations of Ficoll-70 or glycerol. By rearranging Eq. 2.8, we calculated donor–acceptor distances for all of the various environments (see Tables 6.1 and figures 6.3). By doing, so we are able to directly account for changes in refractive index because R_o is depends directly on refractive index (Section 2.8).

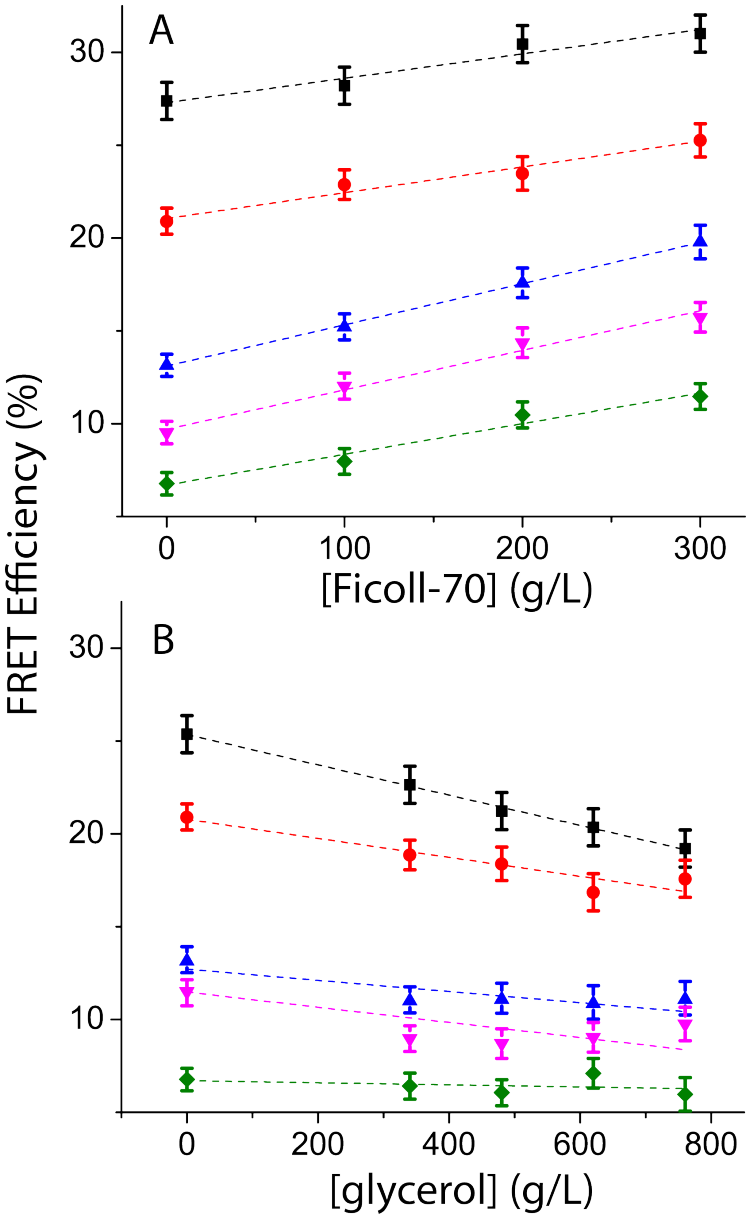

Figure 6.1 FRET efficiency of all constructs, GE (green diamond), E6G2 (pink down triangle), E6 (blue up triangle), G18 (red circle), and G12 (black square) in increasing heterogeneous crowder concentrations (A), and homogenous crowding concentration (B). The dotted line is for visual guidance for trend and not a fit. Error based on 20% the FWHM of the system response function.

6.2.2 Donor-acceptor distance changes upon heterogeneous and homogenous crowding

As discussed in Section 2.8, FRET allows us to calculate the distance between the donor and acceptor. By combining the R_o values that were calculated from steady-state spectroscopy with the FRET efficiencies of each construct and environment, we can calculate R_{DA} using Eq. 6.1.

$$R_{DA}^6 = \frac{R_0^6}{E} - R_0^6 \tag{6.1}$$

These values are shown in Table 6.1. In Figure 6.3A, we observe a decrease in the donor-acceptor distance for all constructs as [Ficoll-70] increases, as we predicted. As we discussed in Chapter 5, the flexible loop regions may form more compact structures even when not in crowding conditions. Figure 6.3 also supports this idea because the G12 and G18 probes, which have linkers consisting only of random coil, have the lowest dynamic range of conformations. Surprisingly, the homogenously viscous environments of glycerol-enriched buffer (Figure 6.3B) show almost no trend in donor-acceptor distance as [glycerol] increases, despite the decreases in FRET efficiency found in Figure 6.1B. This observation may be best explained through two effects: changes in refractive index and a reduction in thermal fluctuations as describe below.

As shown in Figure 6.2 and Table 6.1, the Förster distance in high concentrations of glycerol is much lower than in PBS. In other words, the fluorophores must be closer together to achieve the same FRET efficiency. We had hypothesized little to no conformational changes in the probe under homogenously viscous environments. If we consider the change in R_o due to refractive index changes, we then would expect a decrease in FRET efficiency if there is no conformational change, which is what we observe (Figure 6.1 and 6.3). The decreases in FRET efficiency but little conformational change may also be due to a reduction in thermal fluctuations, as suggested by the Stokes-Einstein model. This reduction would limit the mobility of the entire probe thereby reducing the sampling of favorable dipole-dipole orientations. By analyzing the

donor-acceptor distances, it appears that we can eliminate the complications that refractive index and/or thermal fluctuations might have on FRET efficiency. This assumption is also supported by the fitting parameters discussed in Chapter 4.

6.3 Using Eq. 4.7 for population changes in the constructs

When we revisit the scenarios described in Section 4.1, we can further understand these constructs' responses to macromolecular crowding. We proposed that the proteins have two ways of increasing overall FRET efficiency: increasing the rate of energy transfer of an already established population, or increasing the population capable of FRET by decreasing the donor-acceptor distance. To understand which possibility is occurring, we looked at the pre-exponential factor of Eq 4.6, which is related to the population of constructs capable of undergoing FRET.

As shown in Figure 6.4A, we observe an increase in populations capable of undergoing FRET for four out of five constructs when these proteins are in a heterogeneous environment of Ficoll-70 enriched buffer. Interestingly, the G12 protein, the smallest probe of this family of FRET sensors, does not exhibit an increase in the FRET capable population, rather this population decreases while simultaneously increasing FRET efficiency. These data suggest that the G12 construct increases FRET efficiency by increasing the energy transfer rate, in contrast to the other probes that increase both the population of constructs capable of undergoing FRET and their energy transfer rates. These results also support the idea that a linker, made up of only random coil, is too compact in PBS to allow for a greater dynamic range of FRET efficiencies.

For homogenously viscous environments (Figure 6.2B), we observe no clear trends for the different probes. These results suggest that homogenous environments do not affect their respective populations of FRET-capable probes. These results also suggest that the average donor-acceptor distance does not change due to viscosity.

It is also interesting to examine the relationship between the theoretical donor-acceptor distance (R_{DA}) and the Förster distance. As discussed in Section 2.8, the closer the initial donor-acceptor distance is to the Förster distance, the more sensitive the FRET efficiency becomes to small conformational changes. But this sensitivity appears to come

at a cost of conformational flexibility, which is perhaps best demonstrated by the G18 and G12 probes. These two constructs have the smallest donor-acceptor distance in buffer, but the range of conformations is much lower than the conformational range of the E6, E6G2, or GE constructs.

6.4 Conclusions

This series of five protein constructs has demonstrated dynamic FRET efficiencies in both heterogeneous and homogenous environments. Heterogeneous environments increase FRET efficiencies by decreasing the average donor-acceptor distance, whereas, the constructs in homogenous environments have shown decreased FRET efficiencies. Despite the decrease in FRET efficiency, when combining the results with the Förster distance, we observe no conformational changes in homogenously viscous environments. Additionally, the smaller probes, G18 and G12 appear to have less sensitivity due to a collapsed structure in PBS and therefore cannot become any more compact when in crowded environments. In contrast, the proteins with longer, more rigid linkers are observed to have large dynamic ranges.

Table 6.1 Forster distance and donor-acceptor distance (R_{DA}) for all constructs and environments. Error is not reported due to one measurement of steady-state spectroscopy.

Environment	R_o (nm)	GE (nm)	E6G2 (nm)	E6 (nm)	G18 (nm)	G12 (nm)
PBS	5.26	8.0	7.3	7.2	6.5	6.2
Ficoll-70 100 g/L	5.24	7.7	7.0	6.8	6.3	6.1
Ficoll-70 200 g/L	5.21	7.3	6.7	6.6	6.2	6.0
Ficoll-70 300 g/L	5.14	7.0	6.4	6.4	6.0	5.9
Glycerol 340 g/L	5.19	8.0	7.6	7.3	6.5	6.3
Glycerol 480 g/L	5.14	8.0	7.6	7.1	6.5	6.3
Glycerol 620 g/L	5.09	7.8	7.5	7.2	6.5	6.3
Glycerol 760 g/L	5.06	7.9	7.3	7.1	6.4	6.3

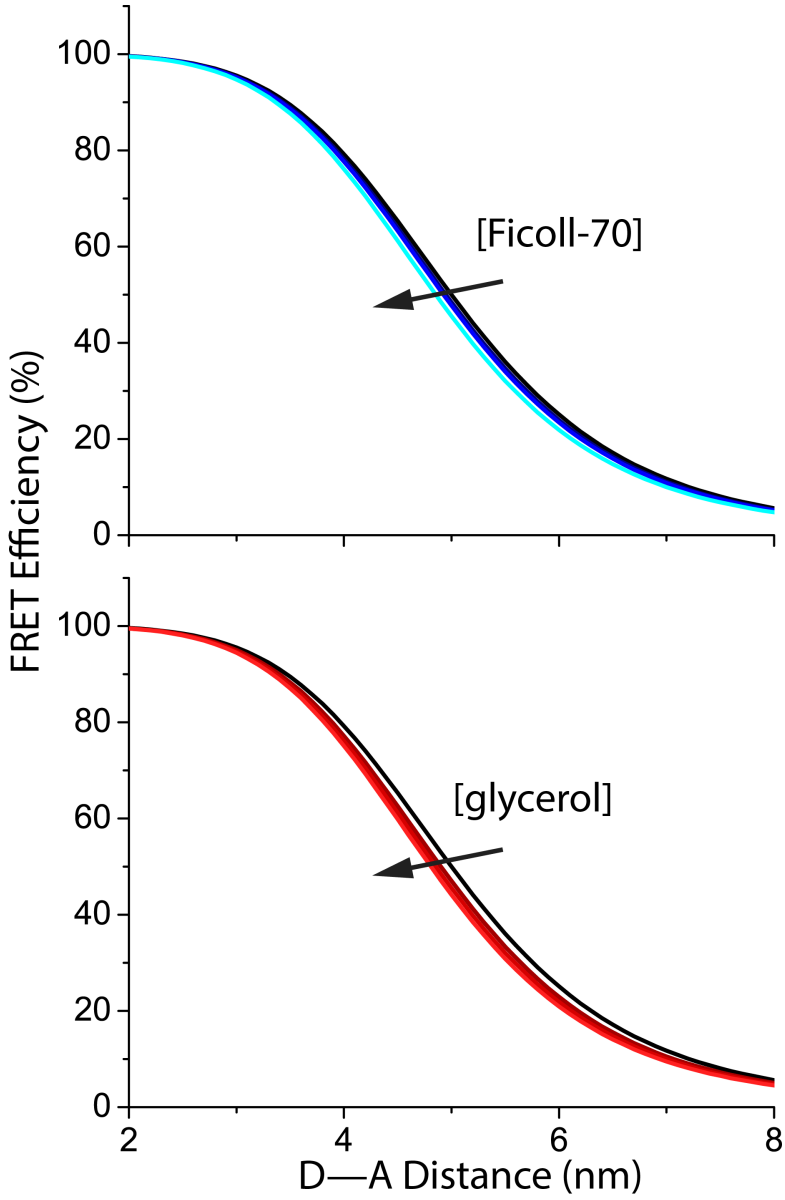

Figure 6.2 Predicted FRET efficiencies for any donor-acceptor distance (R_{DA}). These calculations were calculated using Eq. 6.1, where we estimated R_o using steady-state spectroscopy and refractive index (Table B.1).

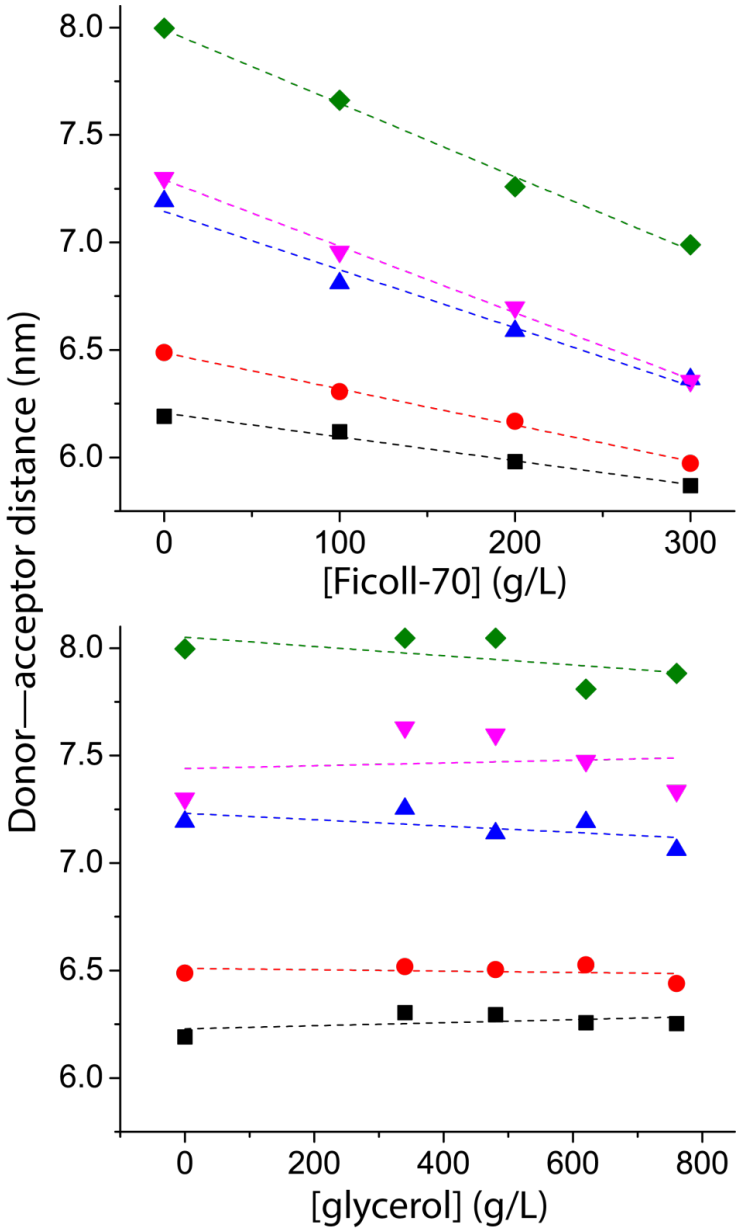

Figure 6.3 Donor-acceptor distance of GE (green, diamond), E6G2 (pink down triangle), E6 (blue up triangle), G18 (red, circle), and G12 (black, square) in various heterogeneous environments (A) and homogenous environments. Error is cannot reported due to only one measurement of steady-state spectroscopy. The dotted line is for visual guidance for trend and not a fit.

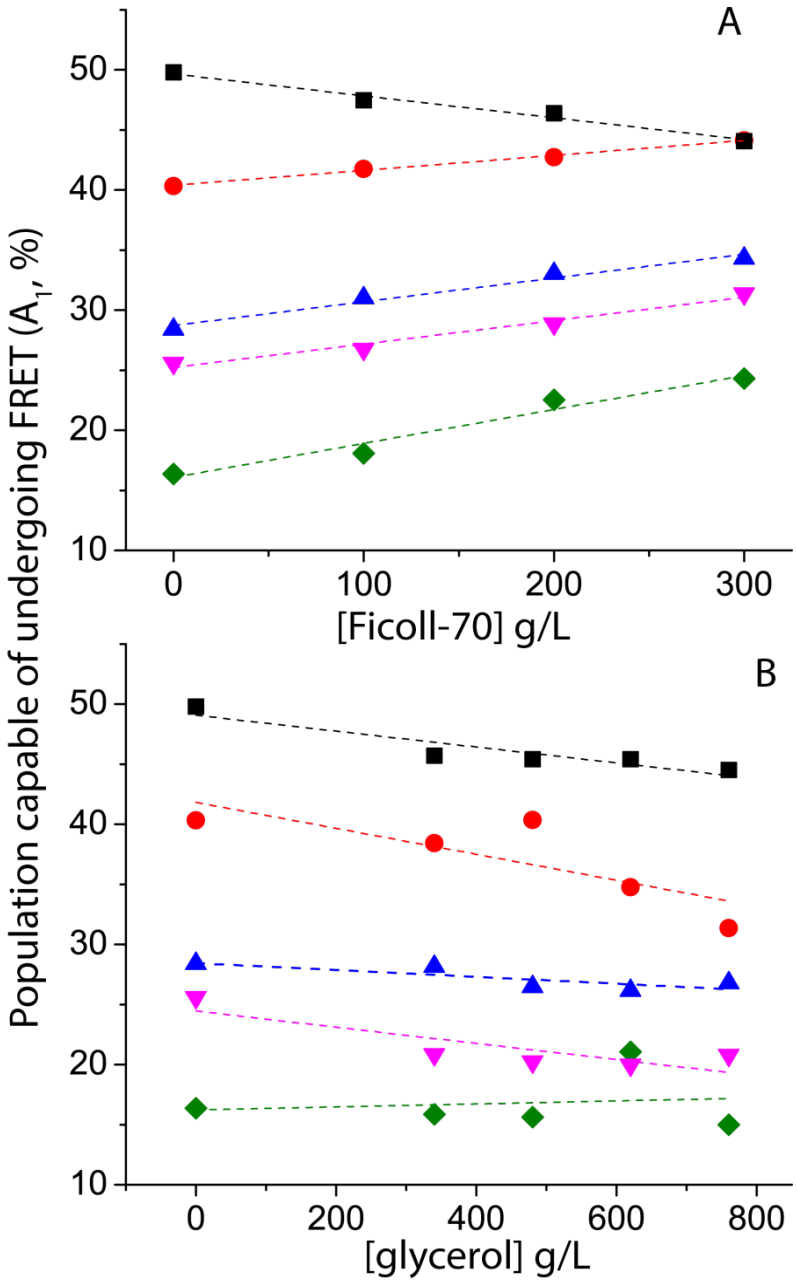

Figure 6.4 Exponential fitting parameters, characteristic of the population capable of FRET in both heterogeneous environments (Panel A) and homogenous environments (panel B). The dotted line is for visual guidance for trend and not a fit. Error is not reported due to limited number of trials.

Chapter 7
Conclusions and future studies

Disclosure: This Chapter has been published, in part, in the following:
Currie, M., Leopold, H., Schwarz, J., Boersma, A., Sheets, E.D., Heikal, A.A. (2017) "Fluorescence Dynamics of a FRET Probe Designed for Crowding Studies" *Journal of Physical Chemistry (B)*.

7.1 Conclusions

In this Thesis, we explored many different aspects of newly developed FRET-based sensors of macromolecular crowding. Steady-state spectroscopy measurements, from both previous studies and the work presented here (Chapter 3), have shown that the FRET efficiencies of these constructs will increase upon exposure to heterogeneous, macromolecular crowding environments. Additionally, we have little to no response to homogenous viscosity. Our ultimate goal is to monitor the effects of macromolecular crowding using these rationally designed proteins *in vivo* as live cells react to various conditions (e.g., the cell cycle) or stimuli (e.g., signal transduction), and steady-state spectroscopy is an impractical technique for *in vivo* studies.

Before we embarked on the time-resolved fluorescence lifetime experiments (Chapters 5), it was essential to have an understanding of the system and how the excited state dynamics of the constructs should react. Therefore, we developed models for populations undergoing FRET or not (Chapter 4), which allowed us to simulate our anticipated experimental results.

We next aimed to further understand these probes using a more non-invasive approach using time-resolved fluorescence lifetime measurements. Initially, we wanted to understand these probes better in the controlled environment of pure buffer (Chapter 5). As expected, linker length and rigidity played important roles for determining the initial FRET efficiency of the probes. FRET efficiency increased with shorter linker length, due to the fluorophores being inherently closer together. Additionally, a more flexible linker also provides more inherent FRET efficiency, as the linkers are able to conform to more compact structures. With respect to the individual constructs, we observed similar trends seen in steady-state spectroscopy when investigating heterogeneous crowding. However,

when using lifetime measurements, these trends in FRET efficiency conflict with previous findings upon investigations into homogenous viscosity, which may be due to the influence of high refractive index on the fluorescence lifetimes.

We had hypothesized that these probes would undergo conformational changes upon heterogeneous crowding and little to no conformational changes upon homogenous crowding. To test this hypothesis, we examined the donor-acceptor distances, in both types of environments (Chapter 3 and 6). By combining the Förster distance (calculated for each environment), with FRET efficiency (Eq. 6.1), we eliminated the influence of refractive index changes. We then could estimate the donor-acceptor distances for each environment. These results are shown in Figure 6.2, where upon Ficoll-70 induced macromolecular crowding, the donor-acceptor distance decreases, confirming the conformational changes due to heterogeneous crowding. Also, despite the decreases in FRET efficiency upon homogenously crowded environments, we can see there is no change in the donor-acceptor distance. This confirms the second hypothesis in regards to conformational changes.

Our results that are described throughout this Thesis suggest that the E6 and E6G2 proteins may be ideal for future *in vivo* studies due to more rigid structure and larger distances between the fluorophores in the absence of crowding agents. This additional rigidity and larger initial distance allows for greater conformational changes to occur upon crowded environments thereby increasing the sensitivities of these two proteins.

7.2 Future directions

The high-impact, potential applications of these constructs are vast, specifically in respect to *in vivo* studies. In addition, due to the ability for genetic encoding into mammalian cells, the next advances we aim to make are incorporating these constructs into living cells. Then by using non-invasive techniques, such as two-photon FLIM (51) , we can begin characterizing these constructs in more complex environments. We are also focusing on the purification of donor and acceptor molecules alone, allowing us to better characterize these fluorophores without complications possibly induced through the cleavage of the probe.

References

1. Ellis, R. J., and A. P. Minton. 2003. Cell biology: join the crowd. Nature 425:27-28.
2. Ellis, R. J. 2001. Macromolecular crowding: obvious but underappreciated. Trends Biochem. Sci 26:597-604.
3. Marenduzzo, D., K. Finan, and P. R. Cook. 2006. The depletion attraction: an underappreciated force driving cellular organization. J. Cell Biol. 175:681-686.
4. Asakura, S., and F. Oosawa. 1958. Interaction between particles suspended in solutions of macromolecules. J. Polym. Sci. 33:183-192.
5. Li, H., S.-X. Dou, Y.-R. Liu, W. Li, P. Xie, W.-C. Wang, and P.-Y. Wang. 2015. Mapping intracellular diffusion distribution using single quantum dot tracking: compartmentalized diffusion defined by endoplasmic reticulum. J. AM. CHEM. SOC. 137:436-444.
6. Li, C., L. M. Charlton, A. Lakkavaram, C. Seagle, G. Wang, G. B. Young, J. M. Macdonald, and G. J. Pielak. 2008. Differential dynamical effects of macromolecular crowding on an intrinsically disordered protein and a globular protein: implications for in-cell NMR spectroscopy. J. AM. CHEM. SOC. 130:6310-6311.
7. Wang, Y., L. A. Benton, V. Singh, and G. J. Pielak. 2012. Disordered protein diffusion under crowded conditions. J. Phys. Chem. Lett. 3:2703-2706.
8. Wang, Y., M. Sarkar, A. E. Smith, A. S. Krois, and G. J. Pielak. 2012. Macromolecular crowding and protein stability. J. AM. CHEM. SOC. 134:16614-16618.
9. Dauty, E., and A. S. Verkman. 2004. Molecular crowding reduces to a similar extent the diffusion of small solutes and macromolecules: measurement by fluorescence correlation spectroscopy. J. Mol. Recognit. 17:441-447.
10. Goins, A. B., H. Sanabria, and M. N. Waxham. 2008. Macromolecular crowding and size effects on probe microviscosity. Biophys. J. 95:5362-5373.
11. Zorrilla, S., M. A. Hink, A. J. W. G. Visser, and M. P. Lillo. 2007. Translational and rotational motions of proteins in a protein crowded environment. Biophys. Chem. 125:298-305.
12. Lavalette, D., C. Tétreau, M. Tourbez, and Y. Blouquit. 1999. Microscopic viscosity and rotational diffusion of proteins in a macromolecular environment. Biophys. J. 76:2744-2751.
13. Zorrilla, S., G. Rivas, and M. P. Lillo. 2004. Fluorescence anisotropy as a probe to study tracer proteins in crowded solutions. J. Mol. Recognit. 17:408-416.
14. Zorrilla, S., G. Rivas, A. U. Acuña, and M. P. Lillo. 2004. Protein self-association in crowded protein solutions: a time-resolved fluorescence polarization study. Protein Sci. 13:2960-2969.
15. Müller, S. M., H. Galliardt, J. Schneider, B. G. Barisas, and T. Seidel. 2013. Quantification of Förster resonance energy transfer by monitoring sensitized emission in living plant cells. Front. Plant Sci. 4.
16. Majoul, I., M. Straub, R. Duden, S. W. Hell, and H.-D. Söling. 2002. Fluorescence resonance energy transfer analysis of protein–protein interactions in

single living cells by multifocal multiphoton microscopy. Rev. Mol. Biotechnol. 82:267-277.
17. Jares-Erijman, E. A., and T. M. Jovin. 2003. FRET imaging. Nat. Biotechnol. 21:1387-1395.
18. Day, R. N., W. Tao, and K. W. Dunn. 2016. A simple approach for measuring FRET in fluorescent biosensors using two-photon microscopy. Nat. Protoc. 11:2066-2080.
19. Koushik, S. V., and S. S. Vogel. 2008. Energy migration alters the fluorescence lifetime of Cerulean: implications for fluorescence lifetime imaging Forster resonance energy transfer measurements. J. Biomed. Opt. 13:031204-031204-031209.
20. Davey, A. M., K. M. Krise, E. D. Sheets, and A. A. Heikal. 2008. Molecular perspective of antigen-mediated mast cell signaling. J. Biol. Chem. 283:7117-7127.
21. Boersma, A. J., I. S. Zuhorn, and B. Poolman. 2015. A sensor for quantification of macromolecular crowding in living cells. Nat. Meth. 12:227-229.
22. Biswas, S., and P. K. Chowdhury. 2015. Unusual domain movement in a multidomain protein in the presence of macromolecular crowders. Phys. Chem. Chem. Phys. 17:19820-19833.
23. Gnutt, D., M. Gao, O. Brylski, M. Heyden, and S. Ebbinghaus. 2015. Excluded-volume effects in living cells. Angew. Chem. Int. Ed. 54:2548-2551.
24. Biskup, C., T. Zimmer, L. Kelbauskas, B. Hoffmann, N. Klöcker, W. Becker, A. Bergmann, and K. Benndorf. 2007. Multi-dimensional fluorescence lifetime and FRET measurements. Micro. Res. Tech. 70:442-451.
25. Duncan, R., A. Bergmann, M. Cousin, D. Apps, and M. Shipston. 2004. Multi-dimensional time-correlated single photon counting (TCSPC) fluorescence lifetime imaging microscopy (FLIM) to detect FRET in cells. J. Microsc. 215:1-12.
26. Wu, P., and L. Brand. 1994. Resonance energy transfer: methods and applications. Anal. Biochem. 218:1-13.
27. Hildebrandt, L. L., S. Preus, and V. Birkedal. 2015. Quantitative single molecule FRET efficiencies using TIRF microscopy. Faraday Discuss. 184:131-142.
28. van den Berg, B., R. J. Ellis, and C. M. Dobson. 1999. Effects of macromolecular crowding on protein folding and aggregation. EMBO J. 18:6927-6933.
29. Minton, A. P. Influence of macromolecular crowding upon the stability and state of association of proteins: predictions and observations. J. Pharm. Sci. 94:1668-1675.
30. Zimmerman, S. B., and A. P. Minton. 1993. Macromolecular crowding: biochemical, biophysical, and physiological consequences. Annu. Rev. Biophy. Biomol. Struct. 22:27-65.
31. Rusinga, F. I., and D. D. Weis. 2017. Soft interactions and volume exclusion by polymeric crowders can stabilize or destabilize transient structure in disordered proteins depending on polymer concentration. Proteins Struct. Funct. Bioinf. 85:1468-1479.

32. Feig, M., I. Yu, P.-H. Wang, G. Nawrocki, and Y. Sugita. 2017. Crowding in Cellular Environments at an Atomistic Level from Computer Simulations. J. Phys. Chem. B.
33. Currie, M., H. Leopold, J. Schwarz, A. J. Boersma, E. D. Sheets, and A. A. Heikal. 2017. Fluorescence Dynamics of a FRET Probe Designed for Crowding Studies. J. Phys. Chem. B. 121:5688-5698.
34. Sarkar, M., C. Li, and G. J. Pielak. 2013. Soft interactions and crowding. Biophys. Rev. 5:187-194.
35. Hall, D., and A. P. Minton. 2003. Macromolecular crowding: qualitative and semiquantitative successes, quantitative challenges. Biochim. Biophys. Acta, Protein Proteomics. 1649:127-139.
36. Kim, J. S., and A. Yethiraj. 2010. Crowding effects on protein association: effect of interactions between crowding agents. J. Phys. Chem. B. 115:347-353.
37. Minton, A. P. 2006. Macromolecular crowding. Current Biology 16:R269-R271.
38. Liu, B., C. Åberg, F. J. van Eerden, S. J. Marrink, B. Poolman, and A. J. Boersma. 2017. Design and properties of genetically encoded probes for sensing macromolecular crowding. Biophys. J. 112:1929-1939.
39. Markwardt, M. L., G.-J. Kremers, C. A. Kraft, K. Ray, P. J. Cranfill, K. A. Wilson, R. N. Day, R. M. Wachter, M. W. Davidson, and M. A. Rizzo. 2011. An improved cerulean fluorescent protein with enhanced brightness and reduced reversible photoswitching. PloS One 6:e17896.
40. Rizzo, M. A., G. H. Springer, B. Granada, and D. W. Piston. 2004. An improved cyan fluorescent protein variant useful for FRET. Nat. Biotechnol. 22:445-449.
41. Shi, X., J. Basran, H. E. Seward, W. Childs, C. R. Bagshaw, and S. G. Boxer. 2007. Anomalous negative fluorescence anisotropy in yellow fluorescent protein (YFP 10C): quantitative analysis of FRET in YFP dimers. Biochem. 46:14403-14417.
42. Marcu, L., P. M. French, and D. S. Elson. 2014. Fluorescence Lifetime Spectroscopy and Imaging: Principles and Applications in Biomedical Diagnostics. CRC Press.
43. Peter, M., S. M. Ameer-Beg, M. K. Hughes, M. D. Keppler, S. Prag, M. Marsh, B. Vojnovic, and T. Ng. 2005. Multiphoton-FLIM quantification of the EGFP-mRFP1 FRET pair for localization of membrane receptor-kinase interactions. Biophys. J. 88:1224-1237.
44. Becker, W. 2014. The BH TCSPC Handbook. Becker & Hickl.
45. Becker, W., A. Bergmann, and C. Biskup. 2007. Multispectral fluorescence lifetime imaging by TCSPC. Micro. Res. Tech. 70:403-409.
46. Lakowicz, J. R. 2006. Principles of Fluorescence Spectroscopy. Springer US Edition 3.
47. Strickler, S. J., and R. A. Berg. 1962. Relationship between absorption intensity and fluorescence lifetime of molecules. J. Chem. Phys. 37:814-822.
48. Dutt, G. 2008. Fluorescence anisotropy of ionic probes in AOT reverse micelles: Influence of water droplet size and electrostatic interactions on probe dynamics. J. Phys. Chem. B. 112:7220-7226.

49. Moriya, T. 1984. Excited-state reactions of coumarins in aqueous solutions. II. The fluorescence quenching of 7-ethoxycoumarins by halide ions. Bull. Chem. Soc. Jpn. 57:1723-1730.
50. Heikal, A. A., S. T. Hess, G. S. Baird, R. Y. Tsien, and W. W. Webb. 2000. Molecular spectroscopy and dynamics of intrinsically fluorescent proteins: coral red (dsRed) and yellow (Citrine). Proc. Natl. Acad. Sci. U.S.A. 97:11996-12001.
51. Yu, Q., and A. A. Heikal. 2009. Two-photon autofluorescence dynamics imaging reveals sensitivity of intracellular NADH concentration and conformation to cell physiology at the single-cell level. J. Photochem. Photobiol., C 95:46-57.

Appendix A Fitting parameters of all intact and cleaved constructs in heterogeneous and homogenous environments

Each construct was purified at least twice. Fluorescence lifetimes were measured using 425 nm excitation and 475/50 nm detection. The parameters shown in Tables A.1.1-A.1.5 are the average of two trials unless otherwise noted. Table A.1.6 shows the cleaved parameters which were found to decay as a single exponential under 425 nm excitation and 475/50 detection. Error in τ values are reported as 20% the FWHM of the system response function used to fit the decay.

Table A.1.1 Average fitting parameters of the GE constructs in various environments, under 425 nm excitation and 475/50 detection. Error for A_1 and A_2 are not reported due to insufficient number of trials

GE	A_1 (%)	t_1(ns)	A_2 (%)	t_2 (ns)	<t> (ns)	E (%)
PBS	16.36	2.14 ± 0.03	83.64	3.99 ± 0.03	3.69 ± 0.03	7.59 ± 0.6
Ficoll-70 100 g/L	18.07	1.91 ± 0.03	81.93	3.89 ± 0.03	3.53 ± 0.03	9.20 ± 0.7
Ficoll-70 200 g/L	22.54	1.76 ± 0.03	77.46	3.82 ± 0.03	3.36 ± 0.03	12.16 ± 0.7
Ficoll-70 300 g/L	24.31	1.66 ± 0.03	75.69	3.75 ± 0.03	3.24 ± 0.03	13.55 ± 0.7
Glycerol 340 g/L	15.86	2.14 ± 0.03	84.14	3.74 ± 0.03	3.49 ± 0.03	6.79 ± 0.7
Glycerol 480 g/L	15.61	2.15 ± 0.03	84.39	3.63 ± 0.03	3.40 ± 0.03	6.36 ± 0.7
Glycerol 620 g/L	21.05	2.31 ± 0.03	78.95	3.52 ± 0.03	3.27 ± 0.03	7.24 ± 0.8
Glycerol 760 g/L	14.98	1.87 ± 0.03	85.02	3.35 ± 0.03	3.13 ± 0.03	6.62 ± 0.9

Table A.1.2 Average fitting parameters of the E6G2 constructs in various environments, under 425 nm excitation and 475/50 detection. Error for A_1 and A_2 are not reported due to insufficient number of trials

E6G2	A_1 (%)	t_1(ns)	A_2 (%)	t_2 (ns)	<t> (ns)	E (%)
PBS	25.60	2.08 ± 0.03	74.40	3.98 ± 0.03	3.49 ± 0.03	12.22 ± 0.6
Ficoll-70 100 g/L	26.75	1.67 ± 0.03	73.25	3.90 ± 0.03	3.30 ± 0.03	15.30 ± 0.7
Ficoll-70 200 g/L	28.86	1.40 ± 0.03	71.14	3.80 ± 0.03	3.11 ± 0.03	18.23 ± 0.8
Ficoll-70 300 g/L	31.39	1.16 ± 0.03	68.61	3.72 ± 0.03	2.91 ± 0.03	21.60 ± 0.8
Glycerol 340 g/L	20.85	2.09 ± 0.03	79.15	3.68 ± 0.03	3.35 ± 0.03	9.01 ± 0.7
Glycerol 480 g/L	20.24	2.02 ± 0.03	79.61	3.56 ± 0.03	3.25 ± 0.03	8.77 ± 0.8
Glycerol 620 g/L	19.97	1.89 ± 0.03	80.03	3.43 ± 0.03	3.12 ± 0.03	8.97 ± 0.8
Glycerol 760 g/L	20.80	1.74 ± 0.03	79.20	3.28 ± 0.03	2.96 ± 0.03	9.77 ± 0.9

Table A.1.3 Average fitting parameters of the E6 constructs in various environments, under 425 nm excitation and 475/50 detection. 95% confidence interval is reported for A_1 and A_2 using 3 replicates.

E6	A_1 (%)	t_1(ns)	A_2 (%)	t_2 (ns)	<t> (ns)	E (%)
PBS†	28 ± 2	2.12 ± 0.03	72 ± 3	4.00 ± 0.03	3.47 ± 0.03	13.46 ± 0.6
Ficoll-70 100 g/L†	31 ± 2	1.91 ± 0.03	69 ± 2	3.92 ± 0.03	3.30 ± 0.03	15.02 ± 0.7
Ficoll-70 200 g/L†	33 ± 4	1.70 ± 0.03	67 ± 4	3.83 ± 0.03	3.13 ± 0.03	16.00 ± 0.8
Ficoll-70 300 g/L†	34 ± 4	1.51 ± 0.03	66 ± 5	3.75 ± 0.03	2.99 ± 0.03	19.36 ± 0.9
Glycerol 340 g/L†	28 ± 2	2.16 ± 0.03	72 ± 2	3.75 ± 0.03	3.30 ± 0.03	11.40 ± 0.7
Glycerol 480 g/L†	26.5 ± 0.4	2.10 ± 0.03	73.5 ± 0.4	3.63 ± 0.03	3.22 ± 0.03	10.07 ± 0.8
Glycerol 620 g/L†	26 ± 2	2.09 ± 0.03	73.86 ± 0.03	3.51 ± 0.03	3.14 ± 0.03	10.14 ± 0.9
Glycerol 760 g/L†	27 ± 5	1.97 ± 0.03	73.21 ± 0.06	3.37 ± 0.03	3.00 ± 0.03	10.31 ± 0.9

Table A.1.4 Average fitting parameters of the G18 constructs in various environments, under 425 nm excitation and 475/50 detection. Error for A_1 and A_2 are not reported due to insufficient number of trials. (*) indicates only one valid trial is available

G18	A_1 (%)	t_1(ns)	A_2 (%)	t_2 (ns)	<t> (ns)	E (%)
PBS	40.34	1.78 ± 0.03	59.66	3.97 ± 0.03	3.09 ± 0.03	22.25 ± 0.7
Ficoll-70 100 g/L	41.79	1.60 ± 0.03	58.21	3.89 ± 0.03	2.93 ± 0.03	24.60 ± 0.8
Ficoll-70 200 g/L	42.75	1.42 ± 0.03	57.25	3.79 ± 0.03	2.78 ± 0.03	26.73 ± 0.9
Ficoll-70 300 g/L	44.16	1.30 ± 0.03	55.84	3.72 ± 0.03	2.65 ± 0.03	28.73 ± 0.9
Glycerol 340 g/L	38.46	1.75 ± 0.03	61.54	3.71 ± 0.03	2.96 ± 0.03	20.32 ± 0.8
Glycerol 480 g/L	40.39	1.86 ± 0.03	59.61	3.59 ± 0.03	2.89 ± 0.03	19.46 ± 0.9
Glycerol 620 g/L*	34.78	1.63 ± 0.03	65.22	3.44 ± 0.03	2.81 ± 0.03	18.30 ± 1
Glycerol 760 g/L	31.39	1.53 ± 0.03	68.61	3.30 ± 0.03	2.67 ± 0.03	19.09 ± 1

Table A.1.5 Average fitting parameters of the G12 constructs in various environments, under 425 nm excitation and 475/50 detection. (*) indicates only one valid trial is available. Error for A_1 and A_2 are not reported due to insufficient number of trials

G12	A_1 (%)	t_1(ns)	A_2 (%)	t_2 (ns)	<t> (ns)	E (%)
PBS	49.79	1.62 ± 0.03	50.21	3.98 ± 0.03	2.89 ± 0.03	24 ± 1
Ficoll-70 100 g/L	47.47	1.59 ± 0.03	52.53	3.90 ± 0.03	2.80 ± 0.03	26 ± 1
Ficoll-70 200 g/L	46.39	1.30 ± 0.03	53.61	3.81 ± 0.03	2.65 ± 0.03	30 ± 1
Ficoll-70 300 g/L*	44.08	1.11 ± 0.03	55.92	3.74 ± 0.03	2.58 ± 0.03	31 ± 1
Glycerol 340 g/L	45.72	1.81 ± 0.03	54.28	3.72 ± 0.03	2.84 ± 0.03	22 ± 1
Glycerol 480 g/L	45.42	1.79 ± 0.03	54.58	3.60 ± 0.03	2.78 ± 0.03	20 ± 1
Glycerol 620 g/L	45.41	1.76 ± 0.03	54.59	3.48 ± 0.03	2.70 ± 0.03	20 ± 1
Glycerol 760 g/L	44.51	1.69 ± 0.03	55.49	3.32 ± 0.03	2.59 ± 0.03	19 ± 1

Table A.1.6 Average lifetime values of cleaved constructs. Each value contains error based on 20% the system response function FWHM (± 0.03 ns).

	GE (ns)	E6G2 (ns)	E6 (ns)	G18 (ns)	G12 (ns)
PBS	3.99	3.98	4.00	3.97	3.98
Ficoll-70 100 g/L	3.89	3.90	3.92	3.89	3.90
Ficoll-70 200 g/L	3.82	3.80	3.83	3.79	3.81
Ficoll-70 300 g/L	3.75	3.72	3.75	3.72	3.74
Glycerol 340 g/L	3.74	3.68	3.75	3.71	3.72
Glycerol 480 g/L	3.63	3.56	3.63	3.59	3.60
Glycerol 620 g/L	3.52	3.43	3.51	3.44	3.48
Glycerol 760 g/L	3.35	3.28	3.37	3.30	3.32

Appendix B Refractive indexes and viscosity use for calculations of Strickler-Berg relationship and R_0

Table B.1.1 Refractive indexes and viscosities of various environments as collected by Chang Thao (2013).

	Refractive Index	Viscosity (cp)
PBS	1.33	1.26 ± 0.09
Ficoll-70 100 g/L	1.35	3.36 ± 0.007
Ficoll-70 200 g/L	1.36	10.1 ± 0.4
Ficoll-70 300 g/L	1.38	28.5 ± 0.3
Glycerol 340 g/L	1.38	3.0 ± 0.1
Glycerol 480 g/L	1.39	4.95 ± 0.03
Glycerol 620 g/L	1.41	8.74 ± 0.05
Glycerol 760 g/L	1.42	18.2 ± 0.2